Finite Element Modeling of the Effect of Reflow Porosity on the Mechanical Behavior of Pb-free Solder Joints

by

Vaidehi Jakkali

A Thesis Presented in Partial Fulfillment
of the Requirements for the Degree
Master of Science

Approved November 2011 by the
Graduate Supervisory Committee:

Nikhilesh Chawla, Chair
Kiran Solanki
Hanqing Jiang

ARIZONA STATE UNIVERSITY

December 2011

ABSTRACT

Pb-free solders are used as interconnects in various levels of micro-electronic packaging. Reliability of these interconnects is very critical for the performance of the package. One of the main factors affecting the reliability of solder joints is the presence of porosity which is introduced during processing of the joints. In this thesis, the effect of such porosity on the deformation behavior and eventual failure of the joints is studied using Finite Element (FE) modeling technique. A 3D model obtained by reconstruction of x-ray tomographic image data is used as input for FE analysis to simulate shear deformation and eventual failure of the joint using ductile damage model. The modeling was done in ABAQUS (v 6.10).

The FE model predictions are validated with experimental results by comparing the deformation of the pores and the crack path as predicted by the model with the experimentally observed deformation and failure pattern. To understand the influence of size, shape, and distribution of pores on the mechanical behavior of the joint four different solder joints with varying degrees of porosity are modeled using the validated FE model.

The validation technique mentioned above enables comparison of the simulated and actual deformation only. A more robust way of validating the FE model would be to compare the strain distribution in the joint as predicted by the model and as observed experimentally. In this study, to enable visualization of the experimental strain for the 3D microstructure obtained from tomography, a three dimensional digital image correlation (3D DIC) code has been implemented in

MATLAB (MathWorks Inc). This developed 3D DIC code can be used as another tool to verify the numerical model predictions. The capability of the developed code in measuring local displacement and strain is demonstrated by considering a test case.

DEDICATION

To my father, Late Chidamber Govind Jakkali

ACKNOWLEDGMENTS

I would like to thank, first and foremost, my advisor Dr. Nikhilesh Chawla for his constant support and encouragement. I am extremely grateful to him for giving me the opportunity to work on this project. Working under his guidance has been a wonderful experience. I sincerely thank Dr. Hanqing Jiang and Dr. Kiran Solanki for their support. I am grateful to the High Performance Computing Center (HPC) for their help in running the high power finite element simulations. I would like to thank all my lab mates for providing timely inputs throughout my thesis.

Last but not the least I would like to thank my family for constantly encouraging me to pursue my interests. I am what I am because of them. I also would like to thank all my friends who have stood by me at all times. This day would not have been possible without your help.

TABLE OF CONTENTS

Page

CHAPTER Page

LIST OF TABLES

LIST OF FIGURES

Figure Page

Chapter 1

INTRODUCTION

1.1 Introduction

Solders are commonly used as interconnects in various levels of electronic packages. At the first level, they are used to connect the silicon chip to the chip carrier and at the second level; they are used to connect the chip carrier to the Printed Circuit Board (PCB) as shown in Figure 1. Solder joints not only provide electrical conductivity between the components but also provide mechanical integrity to the package. Thus, reliability of the package is affected by the mechanical performance of the solder joints. As the solder bump size and pitch continue to decrease due to miniaturization of electronic packages, the micro-structural defects present in the joint become increasingly important for ensuring reliability. One such defect commonly observed in solder joints is voiding. Voids are introduced in the joint during the manufacturing process. These voids can be divided into the following categories: macro-voids, planar micro-voids, shrinkage voids, pin-hole voids, and Kirkendall voids (Aspandiar 2005). Out of the different void types, macro voids are the largest (> 100μm) and a major reliability risk to the solder joints. These voids are generated during the manufacturing process by non-uniform solder shrinkage or by entrapped air resulting from outgassing from the PCB, surface of the components during reflow (Lau and Harkins 1998) (N. C. Lee 2002) (Herzog, Wolter and Poetsch 2003) (Liu and Mei 1994). The size of these voids is relatively large compared to characteristic material length scale. The size and distribution of voids are exacerbated by the presence of micro-vias,

which facilitates air entrapment under the solder paste (Huang, Dasgupta and Lee 2004) (Stafstrom, et al. 2003). Also, now-a-days the traditionally used tin-lead (Sn-Pb) solders are replaced with lead-free solders due to health and environmental concern. Pb-free solder alloys have more voids as compared to their Sn-Pb counterparts (Bath 2003) (Smetana, et al. 2004). Voids in excess of 50% have been observed in some Pb-free solders (Chan, Xie and Lai 1996).

Voiding has been shown to profoundly influence the properties of solder interconnect. It causes weakening of the joint, a loss in ductility due to strain localization around the region of the pores, increased thermal resistivity (Yunus, Srihari, et al. 2007), decreased thermal conductivity (N. Zhu 1999), poor electro-migration resistance (Tang and Shi 2001) and shortens the fatigue life. Several studies in the literature have shown the overall effect of voiding on the failure of the joint but not much work has been done in understanding the effect of different void characteristics namely, size, shape and distribution of voids on crack initiation and propagation in the joint. This thesis is aimed at getting a better understanding of the influence of the different void characteristics on the mechanical performance of the solder joint, by conducting numerical modeling incorporating the actual microstructural features of the joint.

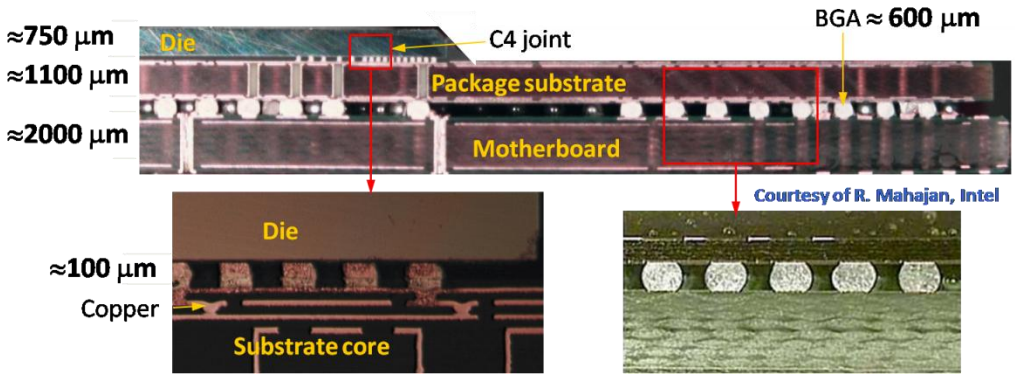

Figure 1 Hierarchy of Electronic Packaging

1.2 Literature Review

Several studies have shown the overall effect of porosity on the mechanical performance of the joint. Lau et al. used mathematical model and Finite Element (FE) analysis to study the effect of voids on stress - strain distribution in 2D rectangular Sn-Pb solder joint (Lau and Harkins 1998). Liu et. al. used analytical model and FE analysis to study the stress distribution in 2D rectangular shape solder for Sn–Pb solders (Liu and Mei 1994). Yunus et al. conducted experiments and 3D modeling for voided Chip Scale Package under mechanical and thermo-mechanical cyclic loadings and found that voids which are greater than 50% of the solder joint area decrease the mechanical robustness of the solder joints. They observed that small voids also affect the reliability, but it is dependent on the void frequency and location (Yunus, Srihari, et al. 2003). Doroszuk et al. studied the effect of voids on thermo-mechanical durability of BGA packages (Doroszuk, et al. 2000). Lau and Erasmus studied the effect of void size, location, and percentage on reliability of Sn–Pb solders for Bump Chip Carrier (BCC) under thermal cycling load using 2D FE models and crack

propagation using fracture mechanics. They concluded that the void size and void location could play important roles on the accumulated inelastic strain of the solder bumps. However, they stated that void percentage less than 20% of the BCC++ solder joint does not affect the reliability of the joint. They also stated that crack propagation could be arrested due to the presence of a void (Lau and Eramus 2002). Zhu et al. conducted experiments and studied the effect of voids on fatigue life of solder. They showed that fatigue life decreases with voiding and is proportional to the ratio of void size to solder resist opening (Zhu, et al. 2003). Herzog et al. investigated the effect of void content on shear strength of the solder joint in chip resistors by experiment. They concluded that void content up to 29% for Sn3.8Ag0.7Cu has no impact on the shear strength (Herzog, Wolter and Poetsch 2003). Kim et al. conducted experiments and modeling for BGA under mechanical cycling. In this study**,** they studied the relationship between formation of voids and fatigue fracture mode and fatigue strength of solder joints was examined using FE analysis and mechanical shear fatigue test. From the results of FE analysis, they found that the equivalent plastic strain and shear strain of solder joints with voids are not always larger than those of solder joints without voids and the magnitude of the strains relate to the position and size of voids in solder joints. Also, the difference of the strains was not much to affect the fatigue strength of solder joints (Kim, Shibutani and Yu 2004). Gonzalez et al. conducted 2D FE modeling of voided solder ball including different size and position of the voids inside the joint and the existence of single and multiple voids. They observed that inelastic strain in case of single void is not much larger than that of

unvoided joint. However, if several voids were located one aside the other, the accumulated strain was much larger (Gonzalez, et al. 2005). Terasaki and Tanie conducted three-dimensional FE modeling of solder joints with spherical and hemispherical voids. Their main conclusion was that the life reduction effect was stronger for hemispherical voids when the void area ratio was higher than 15%. They also conducted 2D FE modeling of the effect of void location on crack propagation. Their calculations revealed that crack propagates from the joint edge towards void center. An increase in distance between the center of the void and the joint interface produced slower crack propagation (Tanie and Terasaki 2005).

However, there are a lot of ambiguities in the results presented in the literature. Most of the modeling has been conducted using 2D FE models and for very limited range of sizes, such as references (Gonzalez, et al. 2005) (Tanie and Terasaki 2005). Also, the modeling is done for very simple 2D rectangular shape joint, such as references (Lau and Harkins 1998) (Liu and Mei 1994). Such simple models are incapable of accurately representing the phenomenon taking place inside the microstructure. Lau et al. (Lau and Eramus 2002) evaluated the reliability of porous solder joints via a finite element analysis under the plane strain assumption. In their analysis, two dimensional circular voids were readily constructed under the plane strain assumption. However, a circular void under the plane strain assumption represents a through-thickness hole instead of a spherical void, which is incorrect in the real situation.

Some authors have incorporated 3D FE models in their analysis (Yunus, Srihari, et al. 2003) (Ladani and Dasgupta 2007) (Yu, et al. 2008). But these

models are an over simplification of the actual geometry and microstructure of the joint. Ladani et al. (Ladani and Dasgupta 2007) have conducted FE analysis of the ball with different void sizes under temperature cycling. They have shown that with increase in void size up to about 15% of the area fraction of the ball, durability increases. For voids bigger than that, the durability starts to decrease. Their conclusions are based on considering the effect of a single void. Practically, however, multiple voids are observed in the joint and the behavior of the joint maybe significantly different when the effect of multiple voids is considered. Q. Yu et al. (Yu, et al. 2008) have studied the effect of void size, location on the fatigue resistance by considering two voids in the joint. Again, this is a huge approximation of the actual scenario, wherein a large number of voids are seen to be randomly distributed in the microstructure. Also, since these models are all simplifications of the actual model, the results obtained cannot be validated experimentally.

None of the studies in the literature have provided detail about the effect of void size and location on damage initiation and propagation. They also provided very limited information about the effect of voids on deflecting the crack from its original path. References (Doroszuk, et al. 2000) (Zhu, et al. 2003) (Tanie and Terasaki 2005) have qualitatively shown that certain percentage of voids is detrimental, but did not provide a quantitative value of the size, location, and distribution of the detrimental voids. Thus, there is a no clear understanding of the influence of void characteristics on the joint reliability. In this study, an

attempt has been made to address the discrepancies in the literature regarding the effect of reflow voids on the failure of the solder joint.

1.3 Focus of the Thesis

This thesis is focused on developing a numerical model incorporating the exact size, shape and location of voids in the solder joint to get a thorough understanding of the influence of different void characteristics and the interplay between them on the mechanical performance of the solder joint. A combined approach of tomography and Finite Element Modeling is utilized to study the effect of reflow porosity on the deformation behavior of a single-lap shear joint composed of Sn-3.9Ag-0.7Cu solder reflowed between copper bars. A lab scale X-Radia Micro XCT is utilized to image the pores in the joint. 3D reconstruction of the exact microstructure is incorporated into an FE model to predict the failure of the joint using a damage model. Interrupted lap shear tests, combined with X-ray tomography, are conducted at different strain levels to visualize the damage evolution within the joint. The FE model is validated by comparing the failure pattern predicted by FE model with experimental results obtained by the interrupted lap shear test. The validated FE model is then used to study the failure of four different solder joints with varying degrees of porosity and different joint geometries.

The tomography technique enables visualization of the deformation of the pores as well as initiation and propagation of crack. However, it cannot be used to visualize the strain distribution inside the joint. To visualize the strain within the microstructure, 3D Digital Image Correlation (DIC) technique has been

implemented in MATLAB. The effectiveness and accuracy of this technique is demonstrated by considering a few test cases.

The thesis is organized as follows: Chapter 2 will discuss the experimental procedure and numerical modeling technique. The results obtained by the FE model and a comparison of the numerical results with the actual experimental observations are presented in the Chapter 3. Chapter 4 will discuss the FE analysis results of four different solder joints with varying degrees of porosity to gain a better understanding of the effect of void characteristics on the failure of the joint. The 3D DIC approach will be discussed in Chapter 5. A summary of the work and future work is presented in Chapter 6.

Chapter 2

NUMERICAL MODELING METHODOLOGY

In this work, a combined approach of X-ray Tomography and Finite Element (FE) Modeling has been employed to study the effect of reflow porosity on the deformation behavior of a single-lap shear joint composed of Sn-3.9Ag-0.7Cu solder reflowed between copper bars. Previous studies by N. Chawla et al. (Chawla, Sidhu and Ganesh 2006) have shown that numerical models incorporating only a simplified geometry of the microstructural features do not accurately reproduce the macroscopic stresses and strains. Indeed, the stress and strain state can only be represented accurately using models that incorporate the true geometry of the microstructural features. Thus, a 3D reconstruction with the exact microstructure of the solder joint was carried out.

Several techniques are available to visualize microstructural features in three dimensions. One of the most widely used techniques is serial sectioning combined with optical microscopy (Sidhu and Chawla 2004) (Dudek and Chawla 2008), or focused ion beam milling (Kubis, Shiflet and Hull 2004) (Singh and Chawla 2010) and image reconstruction to visualize the microstructure in 3D. The destructive nature of serial sectioning however precludes any dynamic analysis, which is essential for studying deformation and failure. X-ray Computed Tomography (CT) is an established technique in the medical field for non-destructive three-dimensional imaging that is growing in popularity in the materials science community (Baruchel, et al. 2008) (Kinney and Nichols 1992). X-ray Microtomography imaging tools with resolution limits below 1μm have

been developed for use with synchrotron as well as lab-scale x-ray sources (Williams, et al. 2010). The non-destructive nature of this technique enables study of the evolution of damage in the material, giving a better understanding of how microstructural features control the damage process (Silva, et al. 2010) (Dudek, et al. 2010).

A lab scale XRadia Micro XCT is utilized to image the pores in the joint. The 3D reconstructed microstructure is incorporated into a FE model to predict the failure of the joint using a damage model. Interrupted lap shear tests, combined with X-ray tomography, were conducted at different strain levels to visualize the damage evolution within the joint. The experimental procedure and the numerical modeling methodology will be discussed in this chapter.

2.1 Joint Preparation and X-Ray Tomography

A single-lap shear joint of Sn-3.9Ag-0.7Cu solder reflowed between copper bars was used in this study. To prepare the joint, a 1 x 1 mm square was cut from 0.5 mm thick sheet of solder. The high-purity Oxygen-free copper bars (approximately 1 mm x 1 mm x 10 mm) were mechanically polished to a 0.05 μm colloidal silica finish, and masked with graphite, leaving a 1 mm x 1 mm area on each bar available for the solder to bond. Immediately prior to reflow, the unmasked region of each copper bar was coated with a thin layer of mildly activated resin flux in order to optimize wetting. The copper bars and solder were then fixed in place using a jig to maintain the alignment of the joint, and reflowed on a hotplate. After reflow, the jig was removed from the hotplate and air-cooled on an aluminum block. This reflow process produced joints with a pore volume

fraction of 4-5 %. The typical pore size distribution, as measured from the 3D reconstructions of the microstructure is shown in Figure 2.

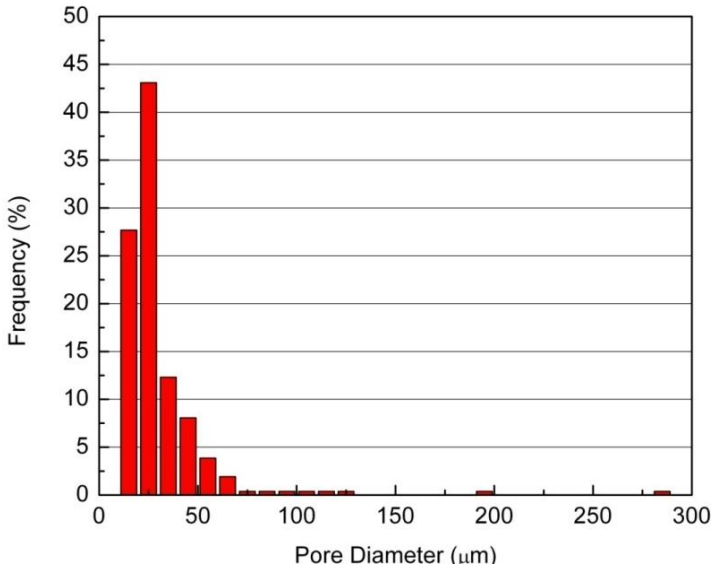

Figure 2 Pore size distribution measured by X-ray tomography (Courtesy E.Padilla)

Microtomography was used to image the solder joint after reflow. A series of 1117 images at 0.25° rotation angle were acquired with a 40 mm specimen-detector distance at an accelerating voltage of 150 kV. This produced a 3D reconstruction of the microstructure with approximately 1μm resolution. After reconstruction in 3D, the dataset was virtually sliced into a stack of parallel cross-sections. Each virtual cross-section was spaced 2.16 μm apart and saved as a Tagged Image File (TIF) image with square pixels of 2.16 μm. Each cubic element (voxel) of the resulting stack represented the absorption contrast of a 10 μm^3 volume.

2.2 Image Segmentation and Reconstruction

The 3D image dataset was segmented using commercial tomographic reconstruction software (Mimics, Matertialise, Ann Arbor, MI). Segmentation

was done by dividing the dataset into masks (corresponding to solder, pores, and the background). After segmentation, the body of the solder and each of the included pores were reconstructed in 3D.

2.3 Interrupted Test

To track the solder microstructural evolution during shear deformation, the lap shear joint was first imaged using X-ray Microtomography in the as-reflowed state, and then loaded in shear using a Tytron 250 micro-force testing tool. After the joint had been sheared at 10^{-3} s^{-1}strain rate for a specified time, it was removed from the test fixture and imaged again using X-ray tomography. This process was repeated several times, producing tomographic datasets at 0, .05, .12, .18, and .44 shear strains. After acquisition, the joints were segmented using the livewire algorithm and reconstructed in 3D. Using X-ray tomography to image the joint at intermediate stages of strain allows the progression of deformation predicted by FE model to be compared to the strain localization observed in the sample.

2.4 Numerical Modeling

Finite Element Modeling is a very powerful numerical tool that can be used effectively to understand the deformation behavior of solder (Shen, Chawla, et al. 2005) (Lee, Lee and Jung 1998) (Shen and Aluru 2010). This technique has been utilized in this study to not only model the deformation of the solder joint but also to predict the initiation and propagation of cracks by incorporating a progressive ductile damage model (Dassault Systems Simulia 2010). Emphasis has been laid on understanding the effect of porosity on damage evolution in the solder joint. The simulation results are then compared to the tomographic

observations to determine the accuracy of the model predictions and thus validate the numerical model.

To conduct Finite Element analysis on the sample, the reconstructed model was imported into commercial meshing software (HyperMesh, Version 9.0, Altair Engineering Inc., Troy, MI) to generate a volume mesh. The meshing was done using linear tetrahedral elements (C3D4). Linear elements are preferred in plasticity modeling cases because most plasticity models tend toward hyperbolic behavior. This allows discontinuities to occur in the solution. If the finite element solution is to exhibit accuracy, these discontinuities in the gradient field of the solution should be reasonably well modeled. With a fixed mesh that does not use special elements that admit discontinuities in their formulation, this suggests that the lowest-order elements-the first order elements-are likely to be the most successful, because, for a given number of nodes, they provide the most locations at which some component of the gradient of the solution can be discontinuous (Dassault Systems Simulia 2010).

Meshing was done in such a way that there was a highly refined mesh around the region of all the pores as shown in Figure 3. The mesh was allowed to grow gradually into the matrix so that the total number of elements in the final model did not significantly increase computation time. The final meshed model has 1,728,106 elements. The meshed model was exported to Abaqus (Version 6.10, Dassault Systems Simulia Corp, Providence, RI) for further analysis.

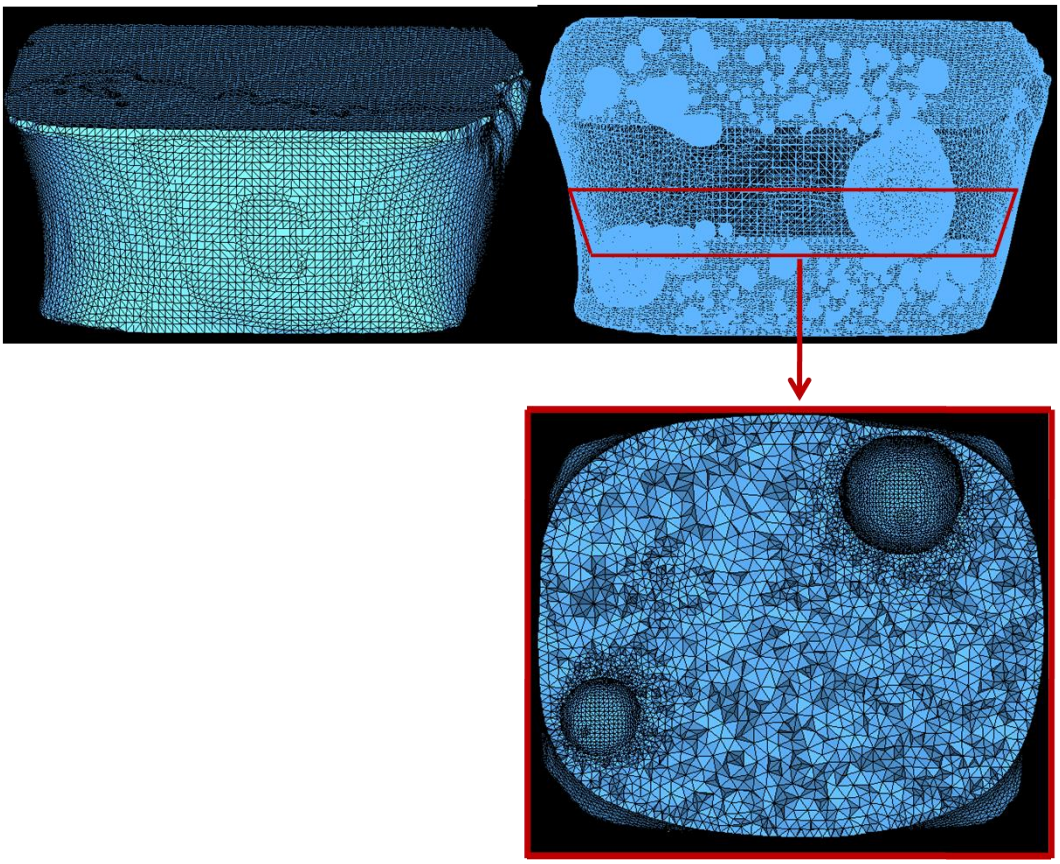

Figure 3 Meshed model of solder showing the highly refined mesh around the pores

The 3D computational model used for the analysis is shown in Figure 4. The solder joint has a thickness of 500μm and an average cross sectional area of 1000x500 μm^2. It is attached to two copper bars at the top and bottom of the joint as in the physical joint. The copper bars are 1000μm x 500μm x 500μm. The copper bar at the bottom is fixed in all the three translational directions whereas the copper bar at the top is fixed in y and z directions and a displacement boundary condition is applied in the x direction to get a pure shear deformation of the solder joint with a nominal strain of 0.9.

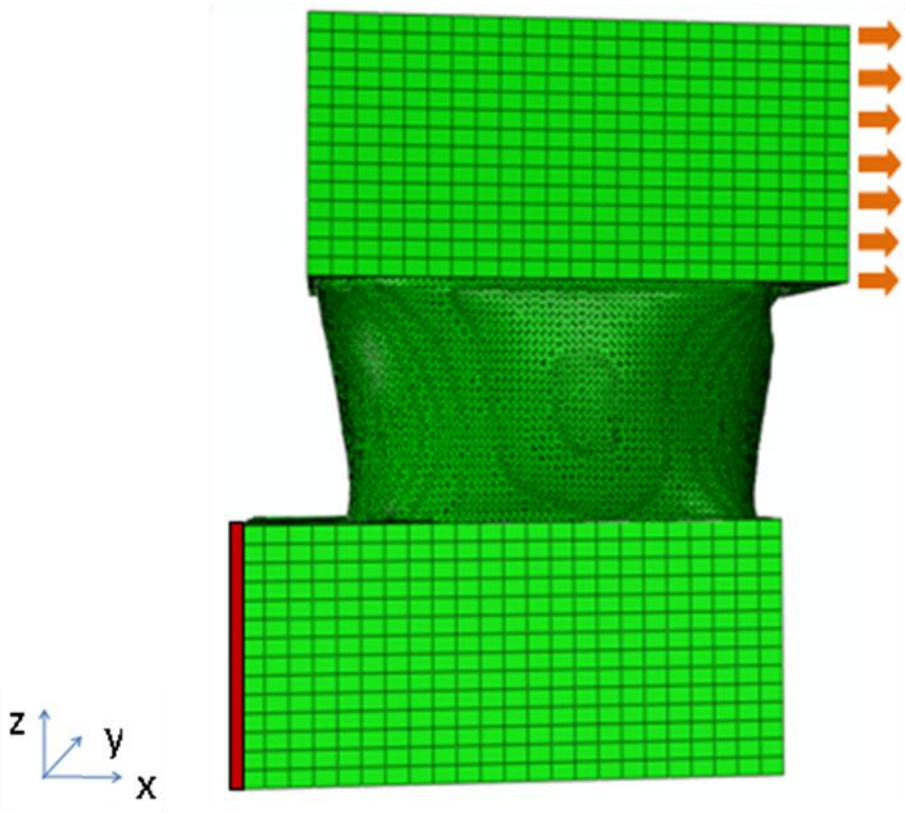

Figure 4 3D computational model used in FE analysis

In the model, the copper bars are taken to be isotropic linear elastic with Young's modulus of 114 GPa, Poisson's ratio of 0.31 and a density of 8,920 kg/m^3. The Sn-3.9Ag-0.7Cu solder was modeled as an elastic-plastic solid with Young's modulus of 48 GPa, Poisson's ratio of 0.33 and a density of 7,290 kg/m^3. The plastic properties of solder were obtained from tensile stress-strain data of Sn-3.9Ag-0.7Cu solder. The plastic properties used for the model are shown in Figure 5. The ultimate tensile strength of the joint was about 38 MPa at a plastic strain of 0.1252 beyond which perfectly plastic behavior was assumed. Though engineering stress-strain curve was used as input for the analyses, a few test runs were also conducted by considering the true stress-strain curve. However, the results did not differ significantly in both the cases.

The model was sheared at 10^{-3} s^{-1} strain rate to simulate quasi-static loading of the joint. ABAQUS explicit solver was employed in the calculations.

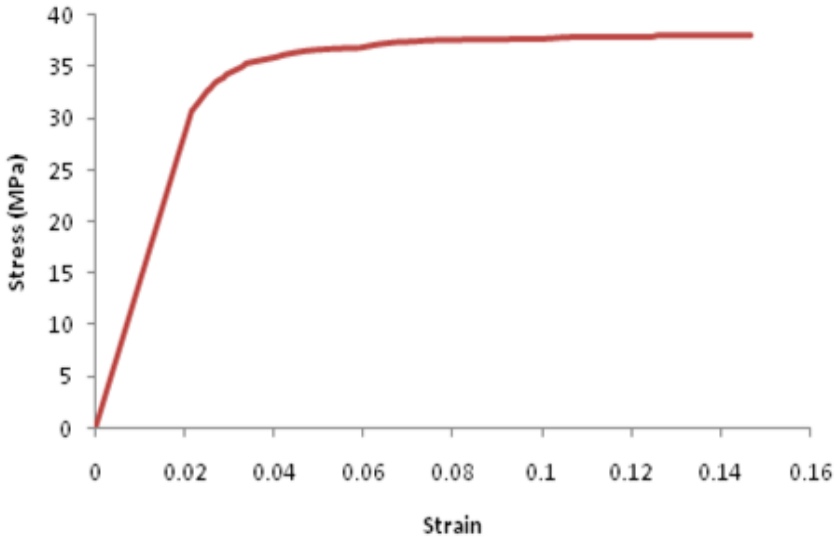

Figure 5 Plastic properties of Sn-3.9Ag-0.7 Cu

The elastic response follows the generalized Hooke's law. Plastic yielding of SAC follows the von Mises criterion and the incremental flow theory (Y. L. Shen 2008). In terms of the principal stresses σ_1, σ_2 and σ_3, the von Mises effective stress is expressed as

$$\sigma_e = \frac{1}{\sqrt{2}}[(\sigma_1 - \sigma_2)^2 + (\sigma_2 - \sigma_3)^2 + (\sigma_3 - \sigma_1)^2]^{\frac{1}{2}} \quad (1)$$

Yielding commences when the magnitude of σ_e reaches σ_y, the yield strength of the metal under uniaxial loading. Note, $\sigma_e = \sqrt{3J_2} = \sqrt{\frac{3}{2}\sigma'_{ij}\,\sigma'_{ij}}$ where, J_2 is the second invariant of the deviatoric stress tensor σ'_{ij} with $\sigma'_{ij} = \sigma_{ij} - \frac{1}{3}\sigma_{ij}\,\delta_{kk}$ (σ_{ij} represents the general stress components and δ_{kk} is the Kronecker delta). Upon yielding, the total strain of an elastic-plastic material, ε_{ij} is the sum

of the elastic part ε_{ij}^{e} and the plastic part ε_{ij}^{p}. The incremental flow theory relates the increment of plastic deformation to stress in the functional form of

$$\sigma_e = f(\int d\bar{\varepsilon}^p) \tag{2}$$

Where, f is the strain hardening function and $d\bar{\varepsilon}^p$, the effective plastic strain increment, is

$$d\bar{\varepsilon}^p = \frac{\sqrt{2}}{3}[(d\varepsilon_1 - d\varepsilon_2)^2 + (d\varepsilon_2 - d\varepsilon_3)^2 + (d\varepsilon_3 - d\varepsilon_1)^2]^{\frac{1}{2}} \tag{3}$$

Where, $d\varepsilon_1, d\varepsilon_2$ and $d\varepsilon_3$ are the principal plastic strain increments. After the material has experienced a plastic deformation history, the equivalent plastic strain (or effective plastic strain) is then

$$\bar{\varepsilon}^p = \int_0^t \frac{d\bar{\varepsilon}^p}{dt} dt \tag{4}$$

Where, t is the time history.

Initially, a basic elastic-plastic simulation was conducted to get an insight into the stress- strain behavior of the joint and to determine the regions of strain localization which are the most likely sites for crack nucleation. The results of the analysis are presented in Chapter 3. The basic analysis enabled identification of the potential sites for crack nucleation and propagation in the model.

The next step of the work was to incorporate a damage model capable of simulating the failure of the joint. The progressive ductile damage model available in ABAQUS was used to simulate the ductile failure of the solder joint. A schematic diagram of the ductile damage response of a material is represented in terms of the stress-strain curve shown in Figure 6. The initial response of the

material is linear elastic and is represented by region 1-2 in the plot. This is followed by plastic yielding of the material in the region 2-3. Beyond point 3, there is reduction in stress carrying capacity of the material with further straining until rupture at point 4. In the absence of damage, the stress in the material would increase with increasing strain beyond point 3 as shown in the region 3-4' of the curve. Point 3 corresponds to the material state at which damage initiates and point 4 is the point at which the material fails completely and has no stress carrying capacity. The region 3-4 of the curve represents the damage evolution path of the material during which gradual degradation of the material stiffness takes place. The damage process is defined in terms of a scalar damage parameter D such that,

$$\sigma = (1 - D)\bar{\sigma} \tag{5}$$

Where σ is the stress tensor in the current increment and $\bar{\sigma}$ is the flow stress in the absence of damage. Thus, at the onset of damage D = 0 and at material failure point D = 1. Once a finite element reaches the material failure point, it is removed and a void is developed in the model. As the material is strained, more elements reach the failure criterion and eventual cracking of the model takes place by the linkage of voids. Thus, the ductile damage response of a material is specified in three parts: the damage initiation point, damage evolution path and the failure point (Dassault Systems Simulia 2010).

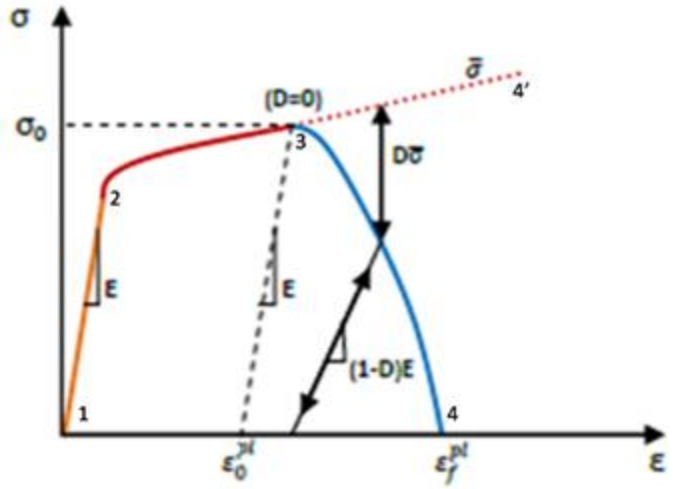

Figure 6 Schematic diagram of Ductile Damage Model (Dassault Systems Simulia 2010)

The ductile damage initiation (D = 0) point, $\bar{\varepsilon}_D^{pl}$ is specified in terms equivalent plastic strain at the onset of damage, $\bar{\varepsilon}_D^{pl}$ which is a function of η and $\dot{\varepsilon^{pl}}$, where $\eta = \frac{\sigma_{hyd}}{\sigma_e}$ is the stress triaxiality, and $\dot{\varepsilon^{pl}}$ is the equivalent strain rate. Here, $\sigma_{hyd} = \frac{1}{3}(\sigma_1 + \sigma_2 + \sigma_3)$ is the hydrostatic stress and σ_e is the effective stress.

In the present study, $\bar{\varepsilon}_D^{pl}$ is assumed to be independent of the stress triaxiality due to lack of experimental data to define the functional form (Shen and Aluru 2010). The strain rate is taken to be 10^{-3} s^{-1} to simulate quasi-static loading of the sample. Once damage sets in, material softening and strain localization take place which display a strong mesh dependency. To alleviate the mesh dependency, a characteristic length is utilized so the softening of the constitutive law is expressed as a strain-displacement relation as detailed below.

The damage evolution law is specified in terms of effective plastic displacement, u_{pl} through the relation

$$u^{pl} = L\varepsilon^{pl} \tag{6}$$

Where L is the characteristic length of an element and is defined as cube root of the integration volume for tetrahedral elements. A linear evolution of damage was assumed so that when the equivalent plastic displacement reaches the failure point, u_f^{pl} the damage parameter D becomes unity. The evolution of damage can be written in terms of the damage parameter as:

$$D = \frac{u^{pl}}{u_f^{pl}} \tag{7}$$

Thus, the ductile damage response is completely specified in terms of two parameters, $\bar{\varepsilon}_D^{pl}$ and u_f^{pl} (Dassault Systems Simulia 2010). In this study, the damage was assumed to initiate at the ultimate tensile strength (UTS) of the material and $\bar{\varepsilon}_D^{pl}$ was chosen to be 0.1252 which is the strain at UTS. The meshed model of the solder joint contained 1,728,106 elements and the characteristic length of these elements varied greatly in the whole model as shown in Figure 3. Such variability in element lengths was inevitable to limit the total number of elements in the final model to a considerate value. Since the range of element lengths was quite wide it was not possible to define an average failure displacement value for all the elements in the model. This would have resulted in the failure of elements with characteristic lengths much greater than the average length at a failure strain much lower than the actual failure strain. Thus, to make all the elements in the model fail at approximately the same strain, different

element groups were created based on their characteristic length. The failure displacement, u_f^{pl} of each element group was calculated separately based on the average characteristic length of every group. The element groups were created in such a way that the maximum deviation in the failure strain from the actual failure strain was less than $\pm$0.07 within every group. The different sub-groups and their failure criteria are listed in Table 1. The failure displacements correspond to an average failure strain of 0.5944. The results of the failure analysis of the model are discussed in chapter 3.

Table 1 Element Sub-groups for ductile damage analysis

Element Subgroup based on characteristic length of the element (μm)	Displacement at failure (μm)	Element Subgroup based on characteristic length of the element (μm)	Displacement at failure (μm)
0.228-0.3	0.156	3-5	2.377
0.3-0.5	0.237	5-8	3.863
0.5-0.7	0.356	8-12	5.944
0.7-1	0.505	12-16	8.321
1-1.5	0.743	16-20	10.699
1.5-2	1.04	20-24	13.076
2-3	1.486	24-28	15.454

Chapter 3

FINITE ELEMENT MODEL VALIDATION

3.1 Finite Element Analysis Results

The solder joint modeling results are discussed in this chapter. To verify the FE model predictions, the analysis results are compared with the interrupted experiment results obtained using X-ray tomography.

3.1.1 Elastic-Plastic Analysis

The plastic equivalent strain (PEEQ) developed in the model by the basic elastic-plastic analysis at a nominal shear strain of 0.33 is shown in Figure 7a. The two large pores near the bottom interface of the joint act as strain localization sites and the highest strain in the model is observed in this region. As the model is sheared further, the strain around the two large pores increased significantly as shown in Figure 7b. Also, the bottom interface is more strained than the top interface. This can be attributed mainly to the fact that the bottom interface has a smaller cross-sectional area than the top interface.

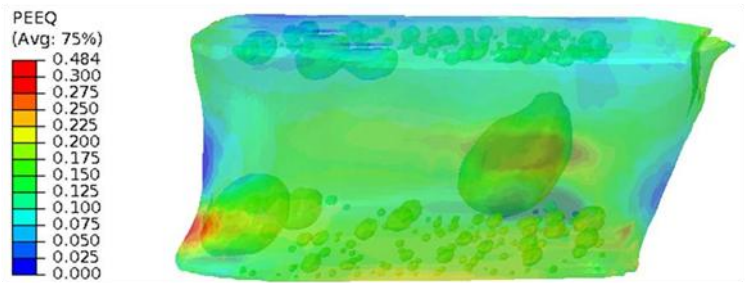

(a)

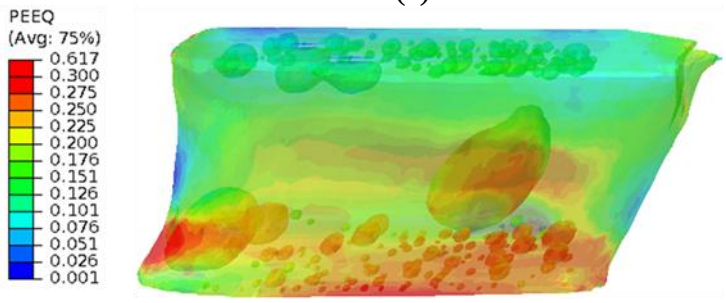

(b)

Figure 7 PEEQ plot at (a) γ= 0.33 (b) γ= 0.45

3.1.2 Ductile Damage Analysis

The elastic-plastic analysis enabled identification of strain localization zones which could act as potential crack nucleation sites in the model. However, the model is incapable of predicting crack growth in the model. To visualize failure of the joint, ductile damage analysis was carried out as described in section 2.4. With the incorporation of the damage model in the FE analysis, stress in the joint initially increases with strain. However, once the damage criterion is met, the stress in the model decreases with further shearing and a crack is initiated when the stress within an element is reduced to zero. A crack is depicted in the FE analysis results by removal of the element. Overall stress-strain response of the entire solder model is illustrated in Figure 8. The stress in the ductile damage model deviates from the elastic-plastic model at a strain of 0.35 and starts

decreasing, indicating that damage has set in the model. With further increase in the shear strain, the stress in the join decreases further.

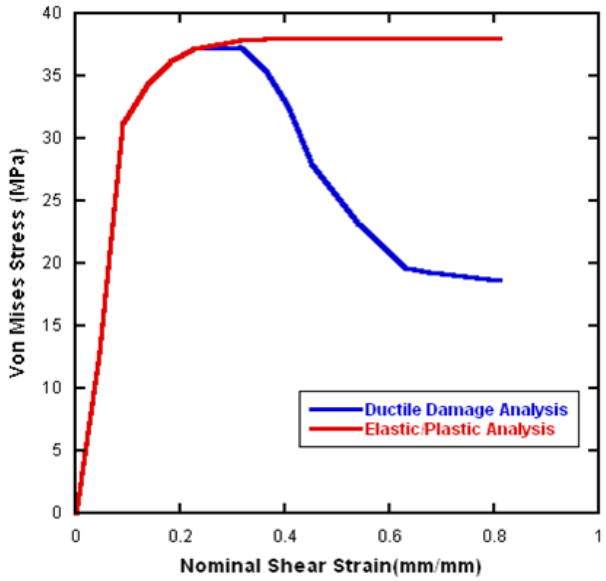

Figure 8 Stress-strain response of the joint

shows the initiation and propagation of cracks in the model. The stress distribution in the entire joint when damage has set in is depicted in Figure 9a. The stress around the vicinity of the two large pores near the bottom interface is lower than the stress away from these pores. This indicates that damage has set in the region around the pores. As the model is sheared further, two cracks are seen to nucleate in the model as shown in Figure 9b. The two cracks observed in the model nucleate adjacent to the two large pores at a strain of 0.39, in the same zone where most of the strain localization was observed in the elastic-plastic analysis. The cracks propagate along the interface linking all the pores and cause eventual failure of the joint. The progression of crack is depicted in Figure 9c.

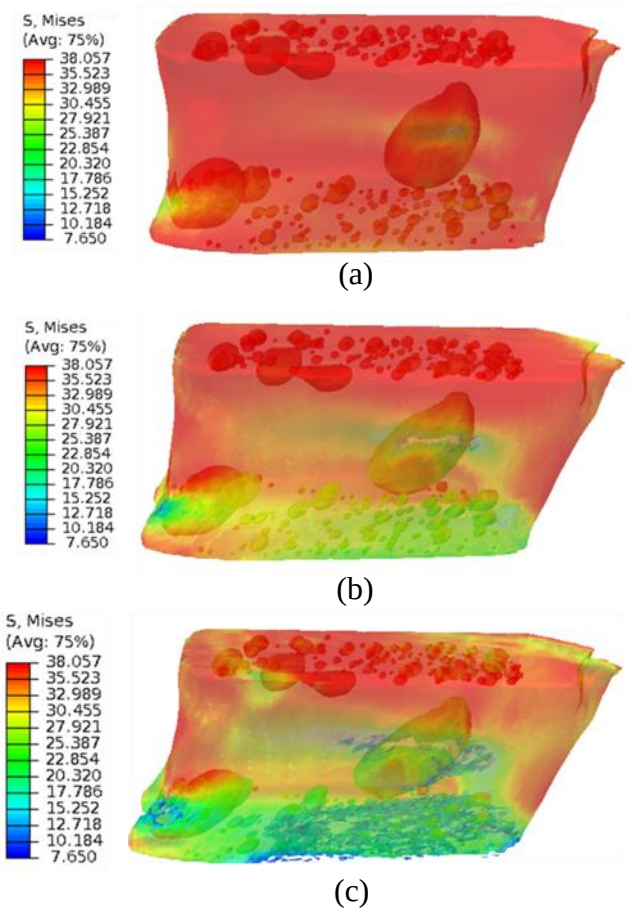

Figure 9 Von Mises stress distribution in the joint for ductile damage analysis at a shear strain of (a) 0.3 (b) 0.39 (c) 0.44

3.1.3 Comparison of Finite Element Analysis results with Experiment

To validate the FE model, the analysis results were compared with tomographic images obtained from the interrupted experiment. Figure 10 shows the deformation of pores observed experimentally and as predicted by the FE model. The FE results show very good correlation with the experiment. In both cases, more pronounced deformation is seen in pores on the lower half of the sample, located near the solder/copper interface. This strain localization correlates with the solder's reduced cross-sectional area near that interface which is approximately 25 % lower than near the opposite interface. The reduction in

surface area is due to both the tapered shape of the solder and the presence of two large (200 μm & 290 μm diameter) pores near that interface.

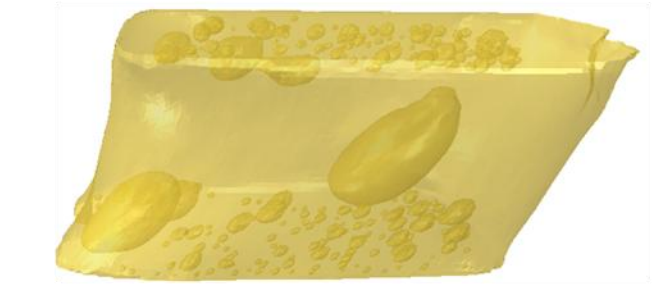

(a)

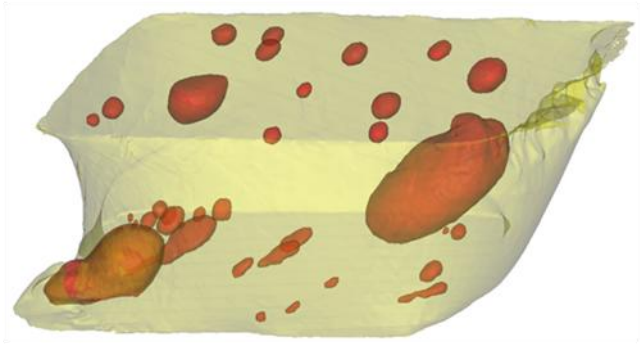

(b)

Figure 10 Deformation of pores at a shear strain of 0.44 as observed (a) in the FE model (b) experimentally

In order to further demonstrate the accuracy of the FE model in predicting deformation of the solder joint, deformation of the largest pore in the model was compared with experiment at different strains as shown in Figure 11. The deformation of the pore observed in the FE results shows very good agreement with the experimental observations, thus indicating the precision of the numerical model in predicting the deformation of the solder joint.

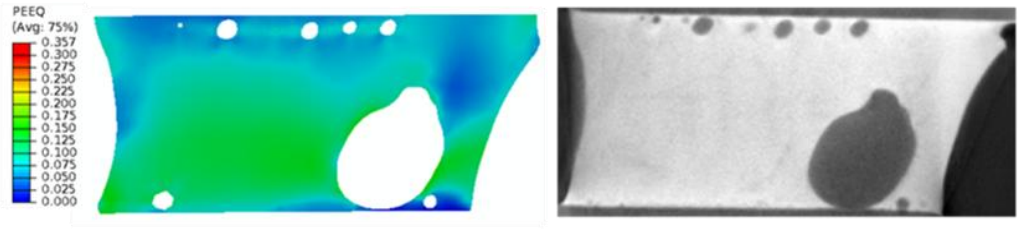

(a)

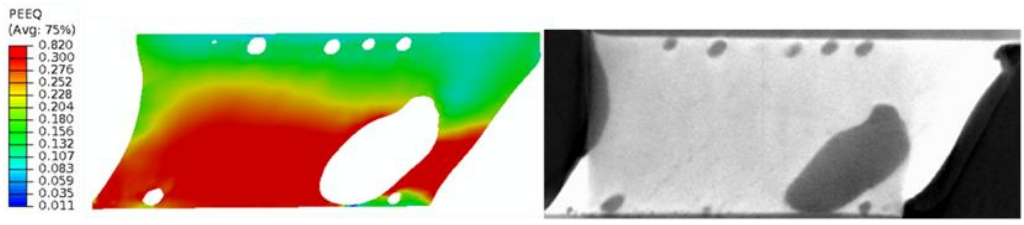

(b)

Figure 11 2D section along the thickness of the joint showing the deformation of the large pore observed in FE simulation (left) and experimentally (right) at a strain of (a) 0.18 (b) 0.44

The numerical model developed should not only predict the deformation of the pores correctly but also represent the failure of the joint accurately. Figure 12 shows a comparison of crack propagation path predicted by FE and observed experimentally. 2-D cross sections across the thickness of the joint depicting the crack in the sample are shown in the figure. The crack around the pore located near the bottom left corner of the joint was predicted to occur in the precise location as observed experimentally. As mentioned in the previous section, FE model predicts crack nucleation at both of the large pores. The crack around the other large pore located at the bottom right corner of the joint occurs in the same location where failure of the pore wall is observed experimentally as shown in Figure 13. Comparison of FE results with experiment clearly demonstrated the capability of the numerical damage model to accurately simulate the deformation as well as the failure of the solder joint.

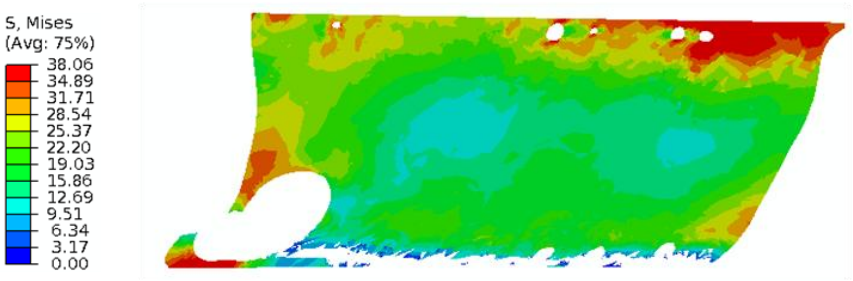

(a)

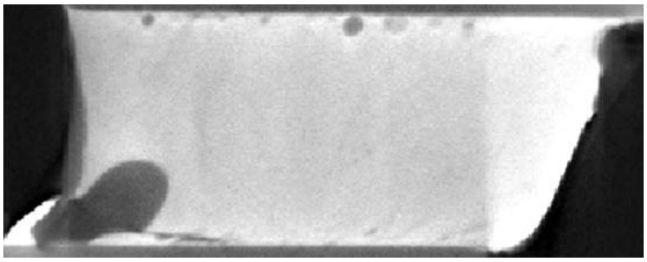

(b)

Figure 12 2D section across the thickness of the joint showing a comparison of propagation of crack (a) as predicted by FE analysis and (b) observed experimentally

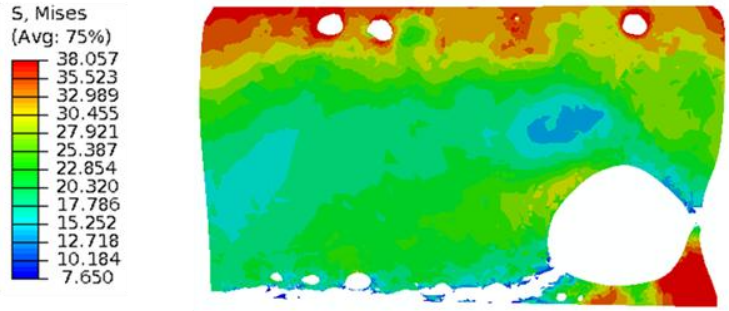

(a)

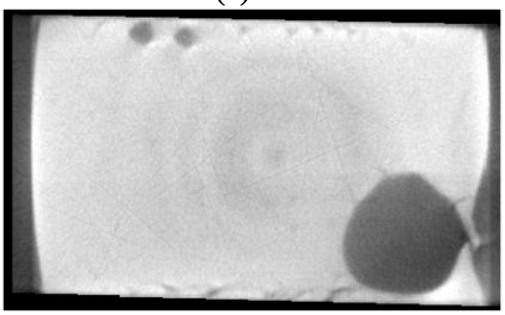

(b)

Figure 13 2D section showing pore wall collapse around the largest pore as observed in (a) FE model (b) experimentally

3.1.4 Effect of porosity

To demonstrate the influence of porosity on the deformation behavior as well as the failure of the joint, ductile damage analysis was carried out by excluding all the pores in the solder and modeling just the solder matrix. Figure 14 shows the comparison of stress distribution in the models with and without porosity along a 2D section taken along the thickness of the joint at different strains. At a strain of 0.11, before the damage has set in the model, the model with porosity has higher stress around the larger pore near the bottom interface whereas the model with no porosity has a homogenous stress distribution in the joint. At a strain of 0.36, the stress in the model with porosity is lower near the bottom interface than the top interface indicating that damage has set in the joint. The model with no porosity on the other hand, is undamaged. As the models are strained further, the model with porosity develops a crack near the large pore at a strain of 0.42 which propagates along the interface linking all the pores. The model without porosity however is still intact and shown no cracking. The model without porosity starts developing a crack at a strain of about 0.69. The model with porosity is completely failed at this point.

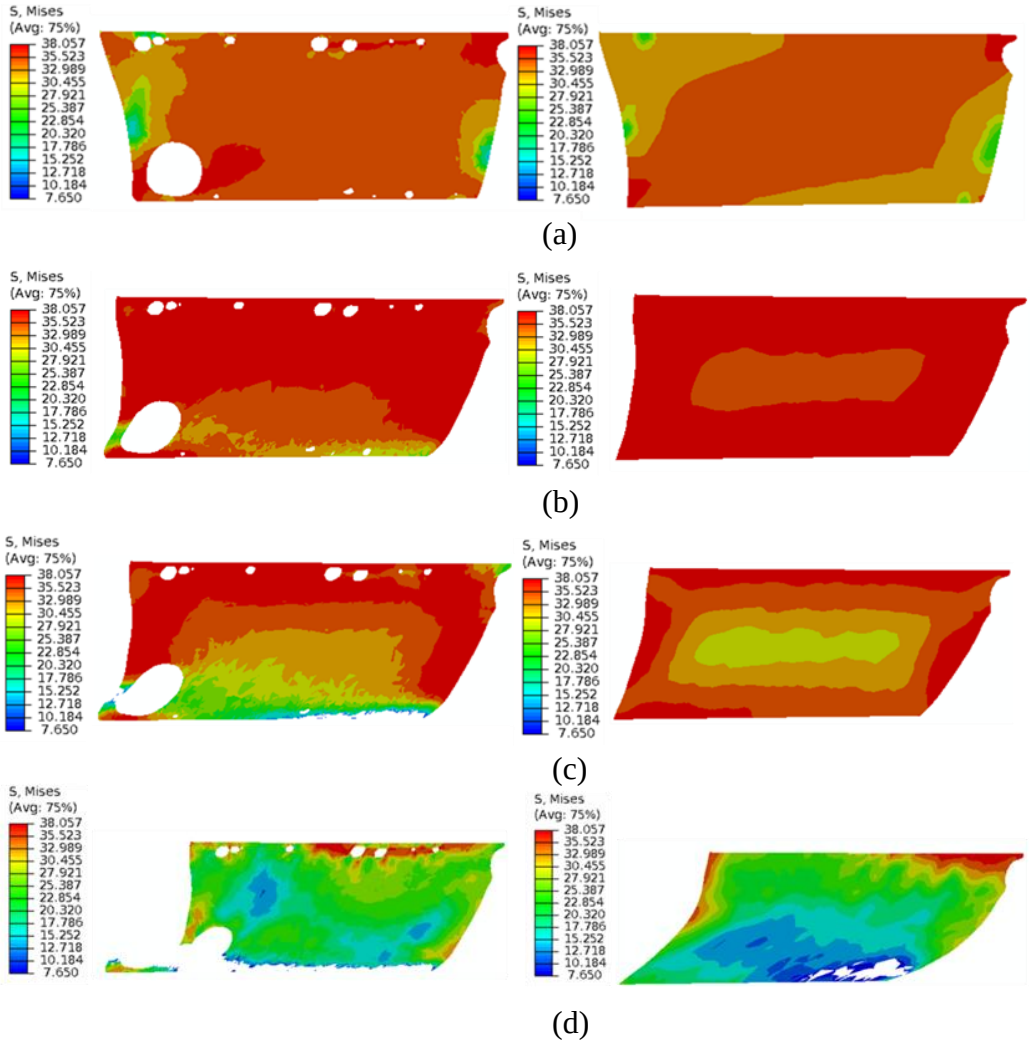

Figure 14 Von Mises Stress distribution and cracking of the model with porosity (left) and without porosity (right) at a strain of (a) 0.11 (b) 0.36 (c) 0.42 (d) 0.62

Chapter 4

FINITE ELEMENT ANALYSIS OF MODELS WITH VARYING DEGREES OF POROSITY

4.1 Introduction

After validating the accuracy of ductile damage model in predicting failure of solder joint, this model was used to study the crack nucleation and propagation path in four different solder joints with varying size, shape and distribution of porosity to understand the influence of the different void characteristics on the failure pattern. The four joints were single lap shear Sn-3.9Ag-0.7Cu solders reflowed between copper bars. The solder joints were prepared by using two different reflow profiles to get varying degrees of porosity in all the joints. The reader is referred to the paper by Chawla et al. (Dudek, et al. 2010) for further details about the experimental procedure.

High resolution X-ray tomography was carried out on the solder joints using Xradia's proprietary MicroXCT technology (Xradia, Concord, California). Once the tomographic data was collected, it was incorporated in tomographic reconstruction software to create a three-dimensional, 16-bit gray scale representation of the sample. The 3D image dataset was segmented using commercial tomographic reconstruction software (Mimics, Matertialise, Ann Arbor, MI). After segmentation, the body of the solder and each of the included pores were reconstructed in 3D. The reconstructed microstructure of all the four solder joint samples is shown in Figure 15. Sample 1 has one large pore near the bottom interface of the joint and a few small pores randomly scattered in the

matrix. Sample 2 has clustering of small sized pores near the top interface. Sample 3 has a distinct geometrical shape with a prominent reduced cross-sectional area in the center of the joint and clustering of medium sized pores near the bottom right edge of the joint. Sample 4 on the other hand has pores larger than Sample 2 and 3 distributed near the top interface.

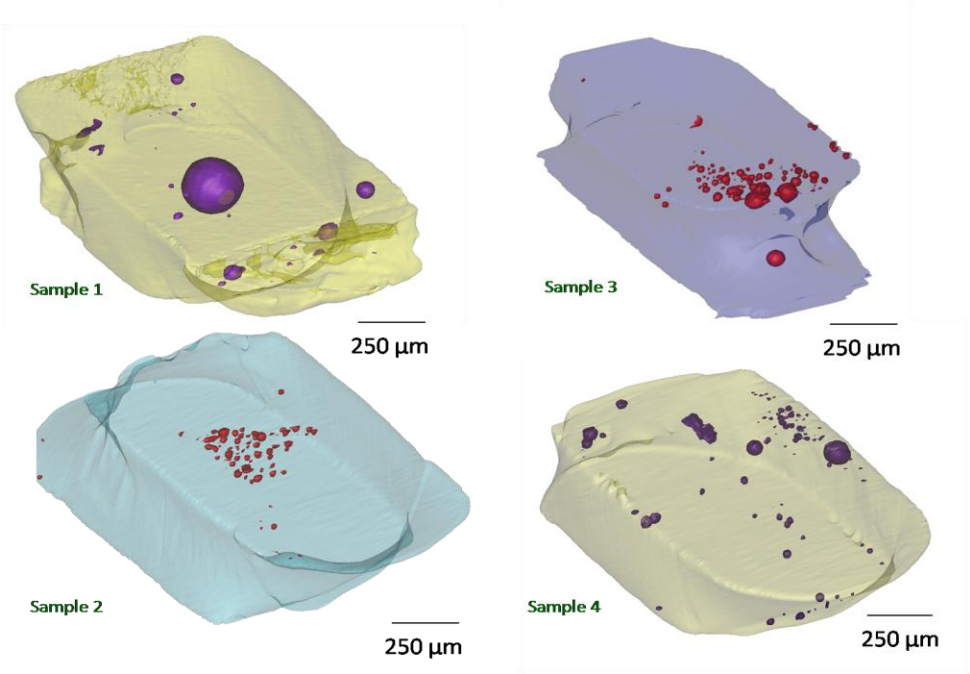

Figure 15 Porosity distribution in all the four samples (Dudek, et al. 2010)

The pore characteristics of all the four joints are summarized in Table 2. Sample 1 has the smallest number of pores but highest volume fraction. Sample 2, 3 and 4 on the other hand have large number of pores but the total void volume fraction is small. All the four joints have unique void characteristics which will clearly lead to a noticeable difference in the strain localization in the joint during mechanical loading and affect the nature of deformation and damage accumulation.

Table 2 Characteristics of porosity in the four samples (Dudek, et al. 2010)

	Sample 1	Sample 2	Sample 3	Sample 4
Number of pores	28	152	61	83
Maximum pore diameter (µm)	206	91	54	94
Pore Volume Fraction (%)	1.1 $\pm$ 0.2	0.06 $\pm$ 0.2	0.4 $\pm$ 0.2	0.2 $\pm$ 0.1

All the samples were meshed in HyperMesh using first order tetrahedral elements (C3D4) to get a highly refined mesh around the pores. The mesh characteristics of all the samples are mentioned in Table 3. These models were analyzed numerically by applying the ductile damage model discussed in chapter 2. The four samples were also analyzed by excluding the porosity in the joint and modeling the solder matrix to clearly visualize the influence of porosity on nucleation and propagation of cracks. The analysis results for all the four samples are presented in this chapter.

Table 3 Mesh Characteristics of the four samples

	Sample 1	Sample 2	Sample 3	Sample 4
Total Number of Elements	65013	366676	561847	368558

4.2 Analysis Results

4.2.1 Sample 1

4.2.1.1 Elastic-Plastic Analysis

The plastic equivalent strain (PEEQ) distribution in the joint for the models with and without porosity at a nominal strain of 0.29 is shown in Figure 16. For both the models, the strain is concentrated at the bottom of the joint. This

is due to the smaller cross-sectional area at the bottom of the joint. The model with porosity has overall higher strain as compared to the model without porosity. Also, in the model with porosity the strain distribution is highly localized around the large pore whereas the model without porosity has a more uniform strain distribution. The strain localization due to presence of porosity plays a significant role in the failure of the model as discussed in the next section.

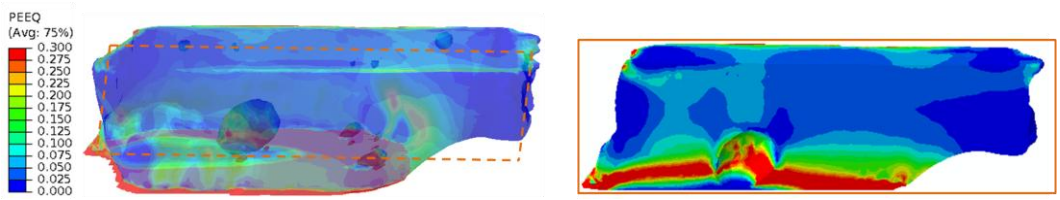

(a)

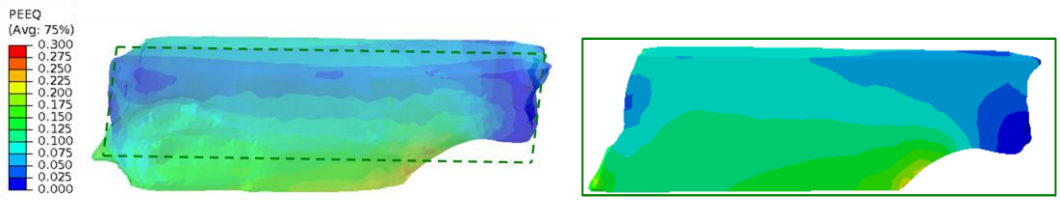

(b)

Figure 16 PEEQ plots of sample 1 for elastic-plastic analysis at γ= 0.29 showing the overall strain distribution in the entire joint (left) and around the region of the large pore (right) for the model (a) with porosity (b) without porosity

4.2.1.2 Ductile Damage Analysis

To visualize the crack propagation behavior of the joint under the influence of porosity ductile damage analysis was carried out. The analysis results are shown in Figure 17. The crack nucleates at the bottom two corners of the joint for the model with porosity at a nominal strain of 0.27 and propagates towards the large pore. As shown in Figure 17a, at a strain of 0.29 the crack has advanced

significantly in the model with porosity however, the model without porosity is entirely intact. As the sample is sheared further, the model with porosity is seen to fail completely at a strain of 0.33 (Figure 17b). The model without porosity on the other hand does not show any crack nucleation. The crack nucleates in this model at a strain of 0.47 which is much larger than the failure strain of the model with porosity. This model fails completely at a nominal strain of 0.56 (Figure 17c)

After the crack nucleates in the model with porosity, it takes a strain increment of 4% for the crack to propagate through the joint and cause complete failure. However, for the model without porosity a strain increment of 9% is required to cause failure of the joint. Thus, presence of porosity not only reduced the failure strain but also increased the crack growth rate for sample 1.

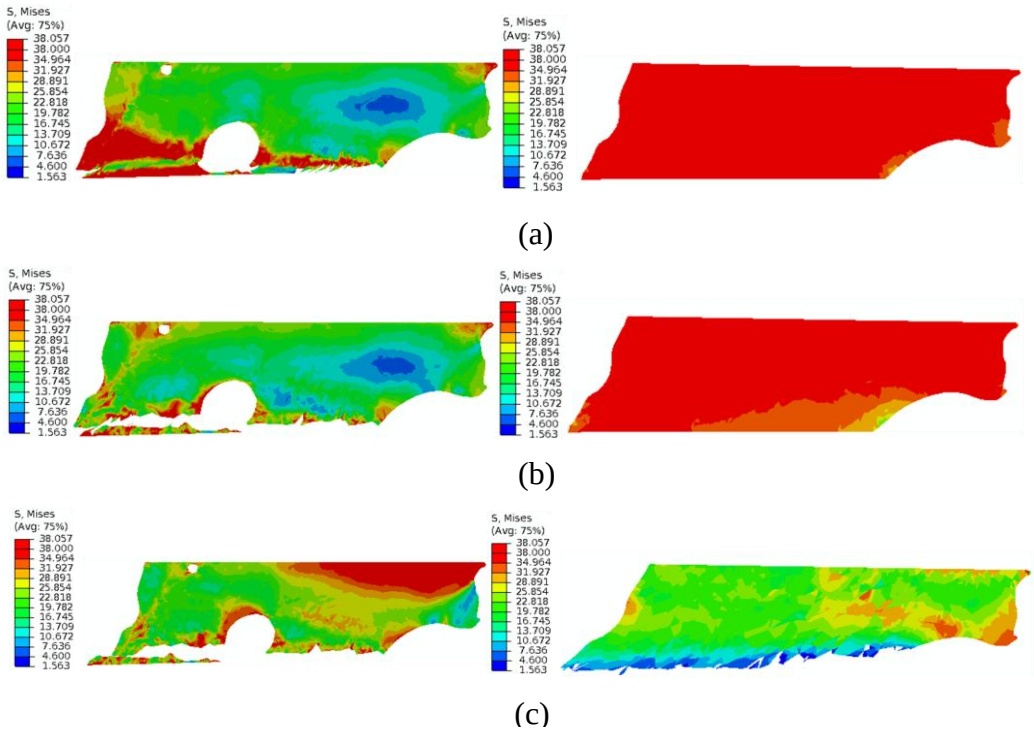

Figure 17 Von Mises stress plot for ductile damage analysis for the models with porosity (left) and without porosity (right) at (a) γ= 0.29 (b) γ= 0.33 (c) γ= 0.56

4.2.2 Sample 2

4.2.2.1 Elastic-Plastic Analysis

The elastic-plastic analysis results are shown in Figure 18 for the models with and without porosity. The 3D strain plots for both the models are very identical. The strain is highest around the top right corner of the joint for both the cases. Sections taken along the thickness of the joint enable a clear visualization of the similarity of strain distribution for both models. No strain localization is observed around the pores. This is because the sample has a very few small sized pores clustered near the top interface. The pore size and pore fraction is not high enough to alter the deformation of the joint.

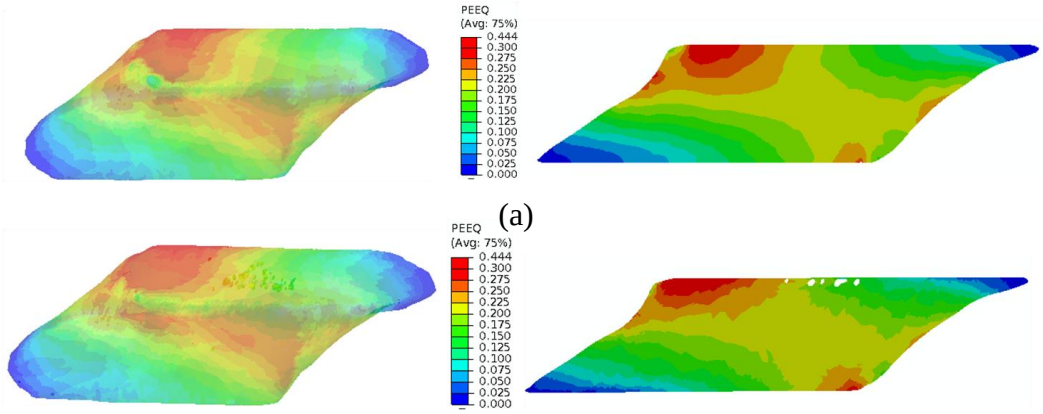

(a)

(b)

Figure 18 PEEQ plot for the model (a) without porosity (b) with porosity at γ= 0.4 for the 3D model (left) and a 2D section along the thickness of the joint (right)

4.2.2.2 Ductile Damage Analysis

The elastic-plastic analysis results clearly showed that the presence of porosity in this case did not affect the strain distribution in the joint. To understand the influence of porosity on the failure of the joint, ductile damage analysis was carried out. The analysis results are presented in Figure 19. The crack nucleates at a strain of 0.45 in both the models near the top right corner of the joint. The elastic-plastic analysis results had shown that this part of the joint was most strained and hence, nucleation of crack in this location validates the accuracy of the ductile damage model in predicting failure. As the models are strained further, the crack propagates along the interface in both the cases and complete failure of the joint takes place at a strain of 0.69.

Thus, in this sample the presence of porosity did not affect the behavior of the joint.

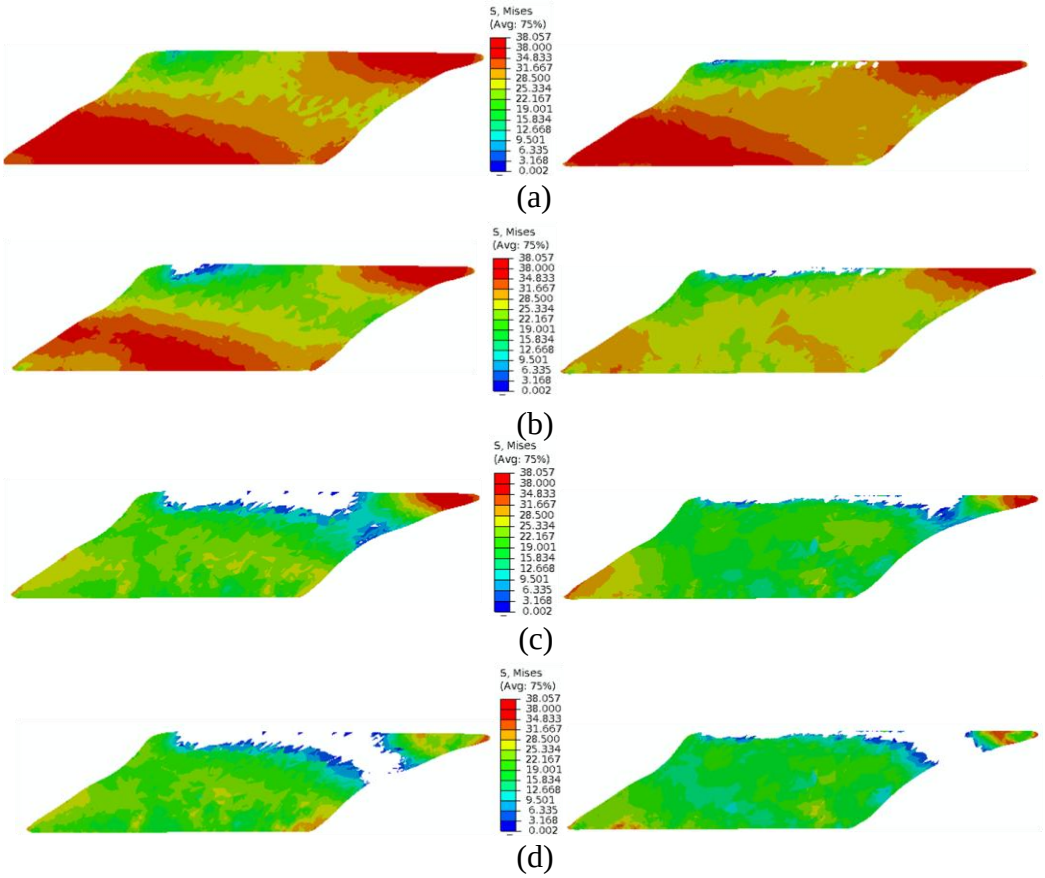

Figure 19 Von Mises stress plot showing crack nucleation and propagation for the models without porosity (left) and with porosity (right) at (a) γ =0.45 (b) γ =0.49 (c) 0.65 (d) 0.69

4.2.3 Sample 3

4.2.3.1 Elastic-Plastic Analysis

The elastic-plastic analysis results for the sample 3 are plotted in Figure 20 at nominal strains of 0.45, 0.54 and 0.6. The strain profiles for the models with and without porosity are very similar. The strain is seen to localize around the center of the joint. This is due to the reduced cross-sectional area in this region. The presence of porosity has not caused a significant increase in the strain concentration. Though the sample has large number of pores near the bottom

interface, the effect of solder geometry seems to have a more prominent effect on the strain localization on the deformation behavior of the joint.

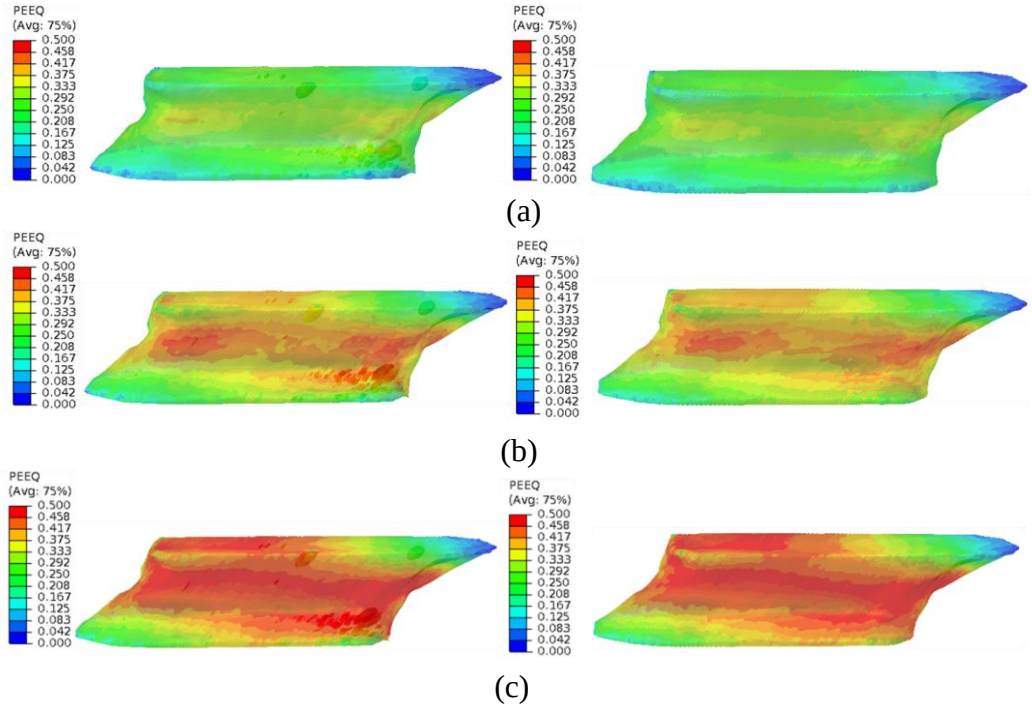

Figure 20 PEEQ plots for sample 3 at a nominal strain of (a) 0.45 (b) 0.54 (c) 0.6

4.2.3.2 Ductile Damage Analysis

The ductile damage analysis results for sample 3 are shown in Figure 21 for the models with and without porosity. In both the cases the crack is seen around the necked part of the joint propagates towards the top interface. The pores in the joint are located near the bottom interface. However, no crack initiation is seen in this region. Also, the failure strain for the models with and without porosity is the same as can be seen in the figure below. This indicates that porosity has no effect on the failure of the joint in this sample. Geometry of the joint governs the crack propagation in this sample.

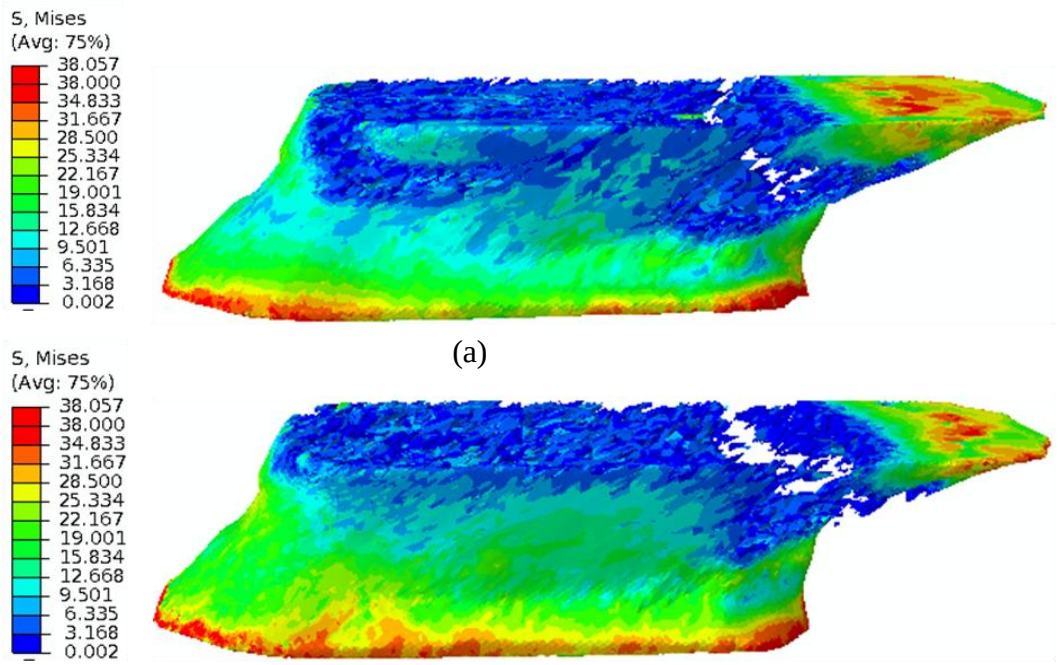

Figure 21 Von Mises Stress in sample 3 at $\gamma = 0.67$ for the model (a) without porosity (b) with porosity

4.2.4 Sample 4

4.2.4.1 Elastic-Plastic Analysis

The 3D plastic strain plots for the models with and without porosity shown on the left in Figure 22 show the overall distribution of strain in the joint. For both the models, the strain is seen to be concentrated around the near the bottom right corner of the joint. This can be attributed mainly to the reduced cross-sectional area in this region. A cross-section taken along the thickness of the joint is shown on the right in the figure to enable a better visualization of the strain field. The bottom right corner of the joint is most strained as mentioned earlier. On the top, for the model with porosity high strain zone is seen along the interface near the

pores. However, the area of strain localization on the top is much smaller than the area at the bottom of the joint.

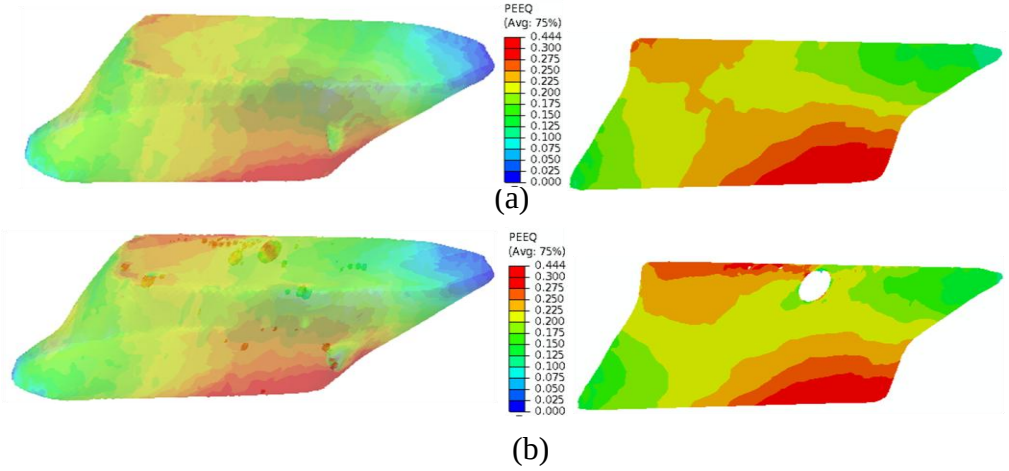

Figure 22 PEEQ plot at γ = 0.4 for the model (a) without porosity (b) with porosity

4.2.4.2 Ductile Damage Analysis

The crack propagation path for the models with and without porosity for sample 4 is shown in Figure 23. The crack is seen to nucleate near the bottom right corner of the joint which propagates along the interface for both the models which corresponds to the region of strain localization predicted by elastic-plastic analysis thus, validating the ductile damage model results. The strains at which the crack nucleates and the rate of propagation is same for both the models indicating there is no influence of porosity on the failure of the joint.

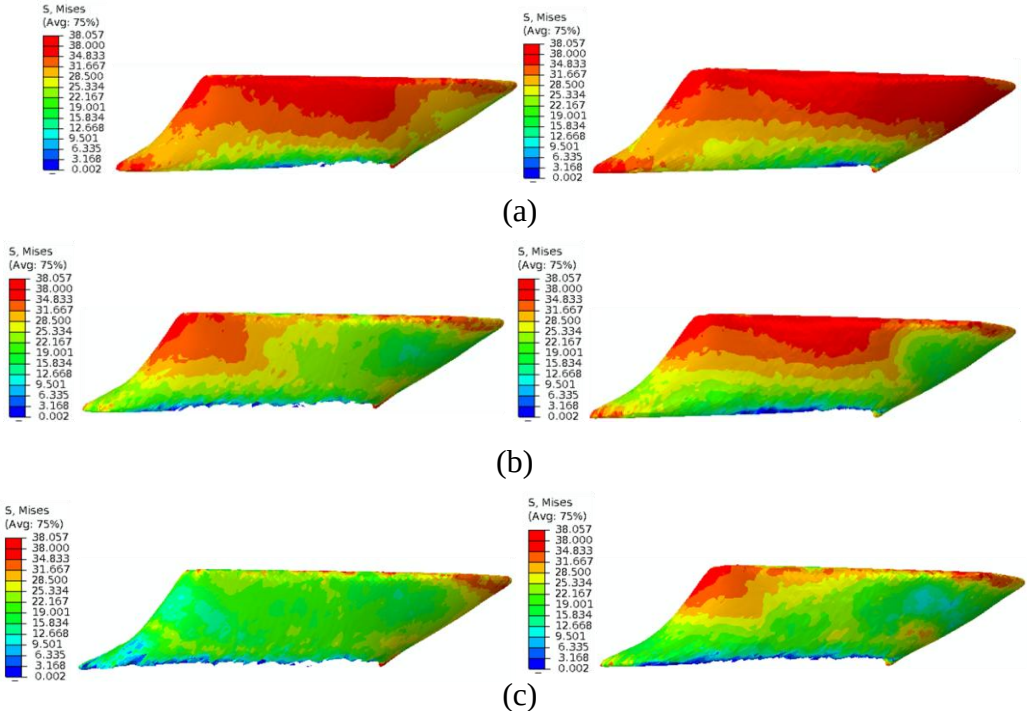

Figure 23 Von Mises Stress Distribution for models with porosity (left) and without porosity (right) at (a) $\gamma = 0.42$ (b) $\gamma = 0.47$ (c) $\gamma = 0.5$

Chapter 5

3D DIGITAL IMAGE CORRELATION

5.1 Introduction

Traditionally, experimental strains have been measured using strain gauges, which performs measurements on isolated points and gives the overall strain in the model. However, this technique is incapable of identifying regions of strain localization in the model. To address this issue and enable full-field deformation measurement, a number of optical measurement techniques such as holography, speckle interferometry and photo-elasticity have been developed for noncontact measurement of displacement and strain fields which are capable of measuring local displacements and strains in the sample. Among those optical measurement techniques, the digital image correlation (DIC) method has gained its popularity, since its invention in the eighties (Peter and Ranson 1982) (Sutton, et al. 1983) (Chu, Ranson and Sutton 1985) largely due to its simplicity in sample preparation and experimental setup and its wide range of measurement sensitivity and resolution (Pan, Qian, et al. 2009). The basic principle of DIC is to match the same physical points imaged in the reference image and the deformed image. To this end, a square subset surrounding the interrogated point in the reference image is selected and used to find its corresponding location in the deformed image. This non-invasive technique has allowed studying behavior of materials and structures in solid mechanics for many applications. Now it has become a powerful tool for quantitative investigation. The technique developed initially allowed to measure displacement and strain only on the surface of specimens during mechanical

loadings. In non-plane loading, the surface of any material is in a state of plane stress whereas within the material, regions of stress triaxiality exist. Thus, surface deformation cannot accurately represent the phenomenon taking place inside the material. Generally, in order to study such complex loading cases numerical tools like finite element simulation are used. However, the obtained results can strongly depend on the chosen mechanical modeling and also on the associated hypotheses (boundary conditions, mesh). Then, the comparison between simulated fields and those obtained on the surface of a similar structure by measurement of displacement or strain can be insufficient to validate the calculus, and the measurement of 3D kinematic fields inside the specimen appears essential in this case (Germaneau, Doumalin and Dupre 2007). Hence, to measure displacements and strains at the core of solids, the 2D DIC technique was extended to three dimensions (Bay, et al. 1998). The 3D DIC technique has been used for applications in medicine, biology as well as to observe heterogeneous materials like ceramics, composites (Phillips and Lanutti 1998) (Maire, et al. 2001) or to detect defects in industrial structures (Benouali, et al. 2002).

In this study, the 3D- DIC technique has been implemented in MATLAB (MathWorks Inc.) to calculate the displacements and strains inside the microstructure. The developed 3D DIC code can be used to validate the finite element results obtained in the previous sections. The accuracy of the developed code to measure 3D strains is demonstrated by considering a model test case.

5.2 Three Dimensional Digital Image Correlation

The displacement field between a reference state and a deformed state of a studied sample is measured on a 3D virtual grid. The displacement of each point of this grid is calculated by inter-correlation of the grey levels of the neighborhood surrounding the considered point in both states. Both the configurations are linked by 3D material transformation. The correlation of grey levels depends on the presence of contrast in the model. The volume images employed in the image correlation are usually obtained by high resolution X-Ray Tomography.

Some materials have inherent contrast due to the density difference between the different phases of the material. However, in materials where such contrast does not exist, artificial markers are introduced in the material which gives the contrast required for the image analysis. The detailed procedure to conduct digital volume correlation of two images is described in this section.

5.2.1 Correlation Coefficient

Measurement of displacement of any point in the reference image, involves finding the best match for the subset of voxels defined around the point of interest in the deformed configuration. The best match is calculated by defining a correlation criterion which determines the degree of similarity degree between the reference subset and its target. The two commonly used correlation criterion are Sum of Squared Differences (SSD) (Lee, et al. 2011) and Normalized Cross Correlation (NCC) (Pan, Qian, et al. 2009) (Verhulp, Rietebergen and Huiskes 2004). The SSD and NCC criteria are defined as:

$$SSD = \frac{\sum_{i,j,k=1}^{N}\{b(x_i^{'}, y_j^{'}, z_k^{'}) - a(x_i, y_j, z_k)\}^2}{\sum_{i,j,k=1}^{N} a(x_i, y_j, z_k)^2} \tag{8}$$

$$NCC = \frac{\sum_{i,j,k=1}^{N} b(x_i^{'}, y_j^{'}, z_k^{'}) a(x_i, y_j, z_k)}{\sqrt{\sum_{i,j,k=1}^{N} a(x_i, y_j, z_k)^2 \sum_{i,j,k=1}^{N} b(x_i^{'}, y_j^{'}, z_k^{'})^2}} \tag{9}$$

Where,

$$x^{'} = x + u + \frac{\partial u}{\partial x}dx + \frac{\partial u}{\partial y}dy + \frac{\partial u}{\partial z}dz \tag{10}$$

$$\mathrm{y}^{'} = \mathrm{y} + \mathrm{v} + \frac{\partial \mathrm{v}}{\partial x}dx + \frac{\partial \mathrm{v}}{\partial y}dy + \frac{\partial \mathrm{v}}{\partial z}dz \tag{11}$$

$$\mathrm{z}^{'} = \mathrm{z} + \mathrm{w} + \frac{\partial \mathrm{w}}{\partial x}dx + \frac{\partial \mathrm{w}}{\partial y}dy + \frac{\partial \mathrm{w}}{\partial z}dz \tag{12}$$

a and b are NxNxN matrices corresponding to subsets in the reference and deformed configuration as shown in Figure 24.

The SSD criterion is sensitive to varying illumination and also cannot find significantly rotated pattern. The NCC criterion on the other hand is insensitive to changes in illumination levels and is more robust. Hence, the NCC criterion is used in the code. The correlation technique involves minimizing the function S by maximizing NCC.

$$S = 1 - NCC \tag{13}$$

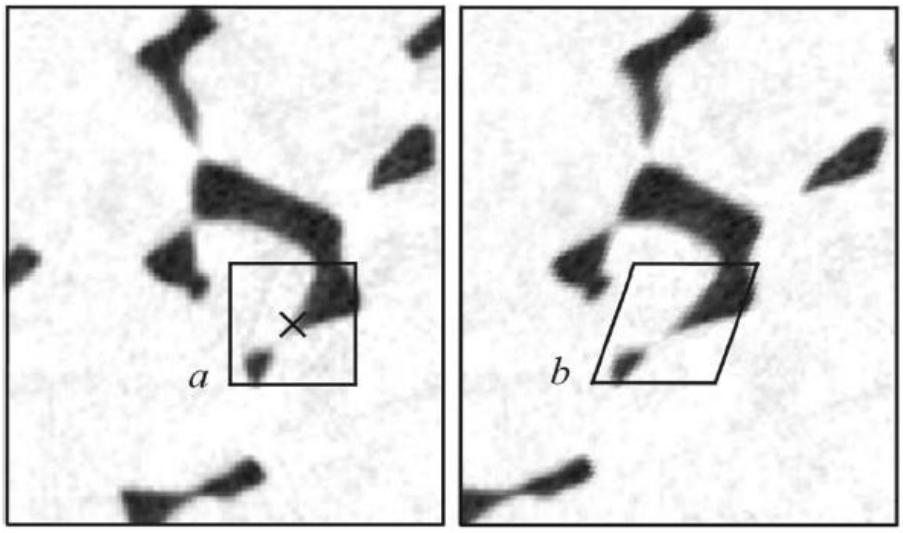

Figure 24 Schematic representation of subsets in the reference and deformed configuration (Verhulp, Rietebergen and Huiskes 2004)

The subset size used for the correlation analysis determines the accuracy of the results. A very large subset size would compromise the spatial resolution of the measured displacement and also increase the computation time. On the other hand, if a very small subset size is used, the feature may not be tracked well resulting in wrong displacement calculation (Jandejsk, Jirousek and Vavrik 2011) (Lee, et al. 2011). Previous studies by Lee et al. (Lee, et al. 2011) have shown a subset size of 21x21x21 voxels is suitable for 3D DIC analysis.

5.2.2 Sub-Voxel Minimization

The function S to be minimized is function of 12 independent variables denoted by the vector D.

$$D\left(u, v, w, \frac{\partial u}{\partial x}, \frac{\partial u}{\partial y}, \frac{\partial u}{\partial z}, \frac{\partial v}{\partial x}, \frac{\partial v}{\partial y}, \frac{\partial v}{\partial z}, \frac{\partial w}{\partial x}, \frac{\partial w}{\partial y}, \frac{\partial w}{\partial z}\right) \tag{14}$$

Minimization of function S is a two step process. In the first step, a voxel level search is carried out to find the best possible match for the template in the deformed image by considering only the translation of the subset i.e. the vector D has only 3 independent variables u, v, and w. The location of the peak of the simplified function corresponds to the displacement components u0, v0 and w0 in whole voxels (Verhulp, Rietebergen and Huiskes 2004). The point under consideration however, could have moved to a sub-voxel location in the deformed image. To determine the sub-voxel displacement of the point, minimization of function S is carried out further with respect to different number of deformation degrees of freedom of vector D. Few studies in the literature have carried out the minimization by considering only 3 degrees of freedom in the model (only translation of the subset included) (Lee, et al. 2011). This method enabled only voxel level correlation between the two images thus, resulting in poor accuracy at high strains. Some other studies included minimization of the correlation function with respect to 6 degrees of freedom of vector D by including the effects of translation and rotation of the subset (Smith, Bay and Rashid 2002). However, the displacement can be measured accurately only if all the 12 degrees of freedom of vector D are included in minimization of function S (Verhulp, Rietebergen and Huiskes 2004). Thus, the code developed in this study included all the 12 degrees of freedom of vector D. With an initial guess as D (u0,v0,w0,0,0,0,0,0,0,0,0,0) minimization is carried out. Tri-linear interpolation is used to evaluate image values between adjacent voxels to enable displacement calculation with sub-voxel accuracy.

5.2.3 Displacement Smoothing and Strain Estimation

The displacement data obtained by the correlation analysis is very noisy. If this data is differentiated to determine the strains, the noise will be amplified resulting in inaccurate strain calculation. Hence, smoothing of the displacement data is carried out before differentiation for strain estimation. The most efficient technique of smoothing the displacement field is by fitting a polynomial to a window of discrete points around the point of interest (Pan, Asundi, et al. 2009). A cube window containing (2m+1) x (2m+1) x (2m+1) discrete points is selected around the point under consideration. If the window is small enough, the displacement within the window can be assumed to be linear and represented as,

$$u(i,j,k) = a_0 + a_1 x + a_2 y + a_3 z \tag{15}$$

$$v(i,j,k) = b_0 + b_1 x + b_2 y + b_3 z \tag{16}$$

$$w(i,j,k) = c_0 + c_1 x + c_2 y + c_3 z \tag{17}$$

Where, i, j and k = -m: m are the local coordinates within the strain calculation window, u(i,j,k) v(i,j,k) and w(i,j,k) are the displacements obtained by the DIC code. The unknown polynomial coefficients a_0, a_1, a_2, b_0, b_1, b_2, c_0, c_1, c_2 are determined from the above equations. Once, the coefficient values are determined, the strain at the center of the window can be calculated by differentiating the displacement equations. This technique gets rid of the noise in the data to a large extent resulting in improved accuracy.

The main parameter to be determined in displacement smoothing is the size of the window. A small window size cannot suppress noise accurately whereas a large window size would result in a highly smoothened field thus suppressing the strain localization in the model particularly for the case of inhomogeneous deformation. Previous studies by Pan et al. (Pan, Asundi, et al. 2009) have shown a strain window size of 11x11x11 is sufficient. This window size has been used in the code.

5.2.4 Post-Processing of Displacement and Strain

After calculating the displacement and strain data by the 3D DIC code, some post-processing of the results is carried out before visualization. The first step involves getting rid of badly tracked markers. This is done by plotting the displacements calculated for all the markers in the model. The outliers are identified manually and are removed from the analysis. After identification of the outliers, the displacement data is smoothened and the strains calculated.

The 3D DIC code gives displacement and strain values at discrete points in the model. The output data needs to be interpolated at the remaining locations in the image. A tri-linear interpolation technique is implemented to interpolate the result data. The 3D contour plots generated by the DIC analysis were visualized using PARAVIEW (Kitware Inc, 2000) software. The step by step process of conducting the correlation analysis of two images is summarized in Figure 25.

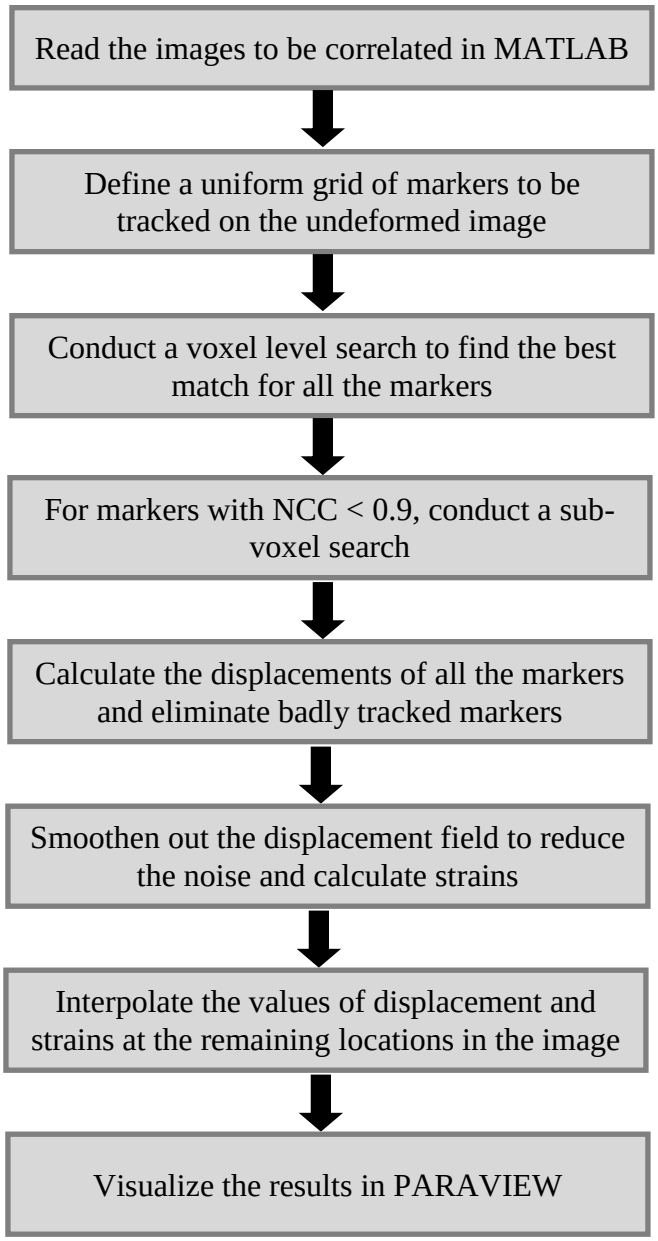

Figure 25 Flow Chart of 3D DIC

5.3 Test Model for Code Validation

To test the accuracy of the 3D DIC code in calculating displacement and strain, a test model was built. The model includes a single spherical pore of radius 15 units embedded in a cube of size 60x60x60 units as shown in Figure 26. This

model was built in ABAQUS (v 6.10). The FE model had 6875 linear tetrahedral elements (C3D4).

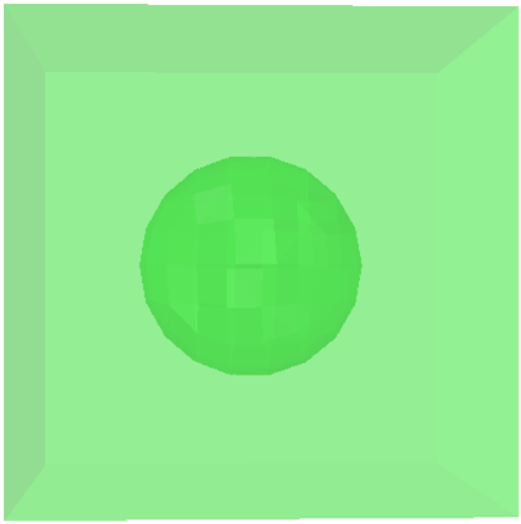

Figure 26 Test Model

The model was deformed numerically by applying a displacement boundary condition to the face on the right and constraining the face on the left as shown in Figure 27 to get a nominal strain of 0.2. The undeformed and deformed configurations obtained by the FE analysis were exported as .STL files. These two images were used as input for the 3D DIC code. The inherent contrast between the intensity levels of the pore and the surrounding matrix was used for tracking in DIC. The image correlation was carried out in MATLAB using the developed code. The displacement and strain plots obtained by the DIC code were compared to the results obtained by the FE analysis to determine the accuracy of the DIC code.

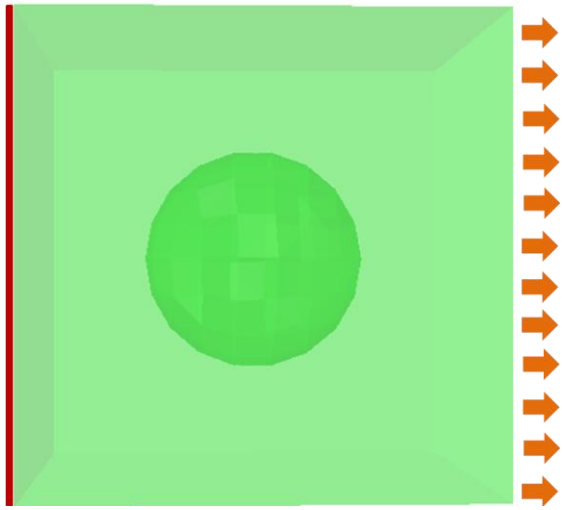

Figure 27 Boundary conditions applied to the test model

5.4 3D DIC Results

DIC analysis was carried out on the undeformed and deformed datasets by tracking about 7515 markers distributed uniformly around the void in the center of the undeformed image. The displacement and strain plots obtained by the DIC analysis are discussed below. Figure 28 shows the z-displacement plots obtained by the DIC analysis and FE model. The displacement profile predicted by the DIC code shows very good correlation with the displacement profile predicted by the FE model. In both the cases, the displacement is increasing from the left edge to the right edge which is the edge being pulled. A comparison of the y-displacement plots is shown in Figure 29. The FE model predicts maximum y-displacement at the top and bottom of the void. The same behavior is also predicted by the DIC code. Thus, the DIC code models the y-displacement quite accurately. The x-displacement plots obtained in both the cases also show a very good match as shown in Figure 30. Thus, the DIC code determines the displacements quite accurately.

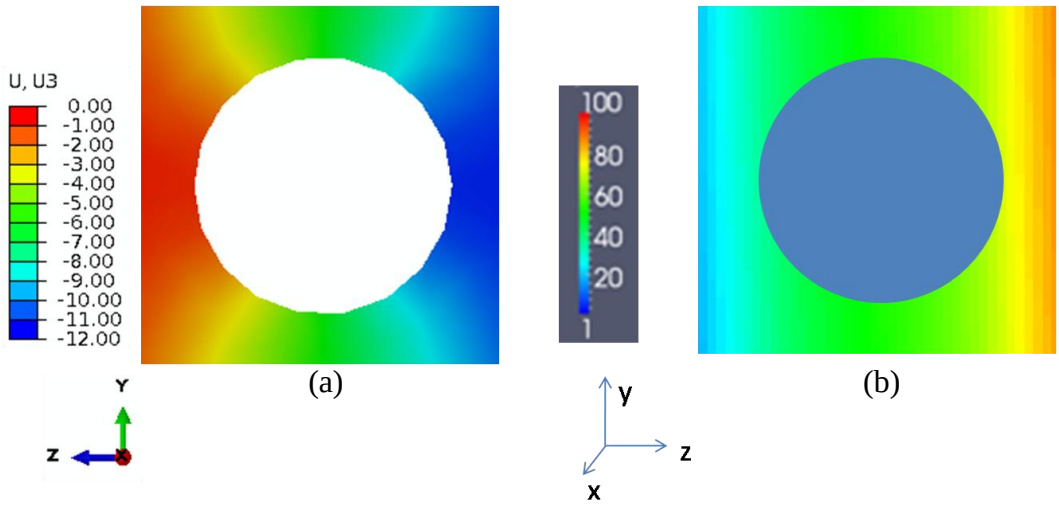

Figure 28 Z- displacement plots as predicted by (a) FE Model (b) DIC code

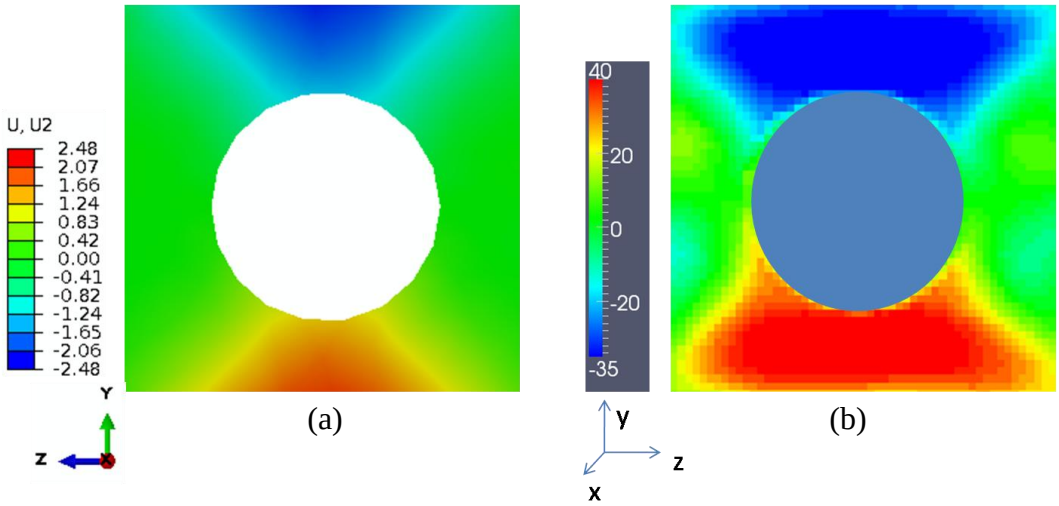

Figure 29 Y- displacement plots as predicted by (a) FE Model (b) DIC code

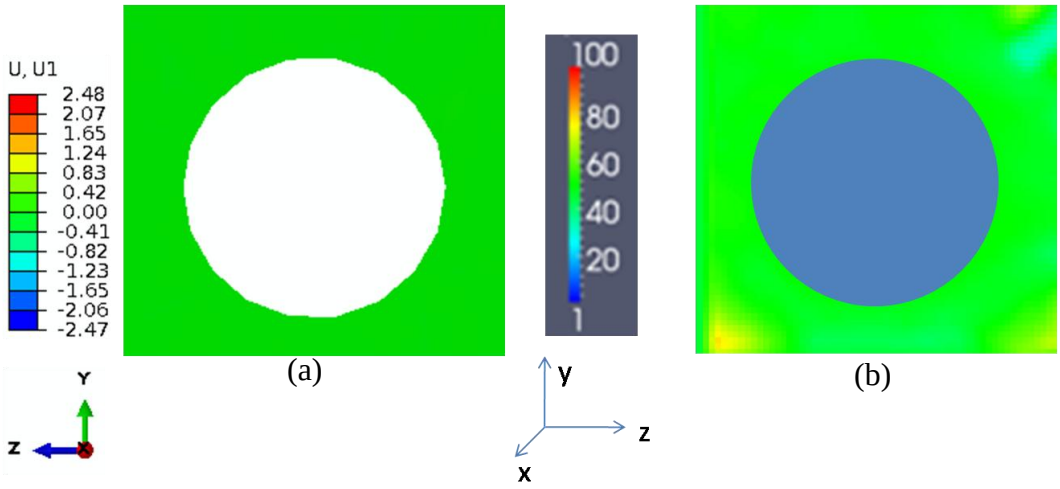

Figure 30 X- displacement plots as predicted by (a) FE Model (b) DIC code

Figure 31 shows E33 strain plots obtained by the DIC code and the FE model. The strain is maximum at the top and bottom of the void in both the cases. The strain profile predicted by the DIC code shows a very good correlation with the strain profile obtained by the FE model. The E22 strain plots also compare very well as shown in Figure 32. The FE model shows maximum strain at the top and bottom of the image indicated by the green colored contour. The DIC code also shows maximum strain in the same location. Thus, the DIC code predicts the displacement and strain contours quite accurately.

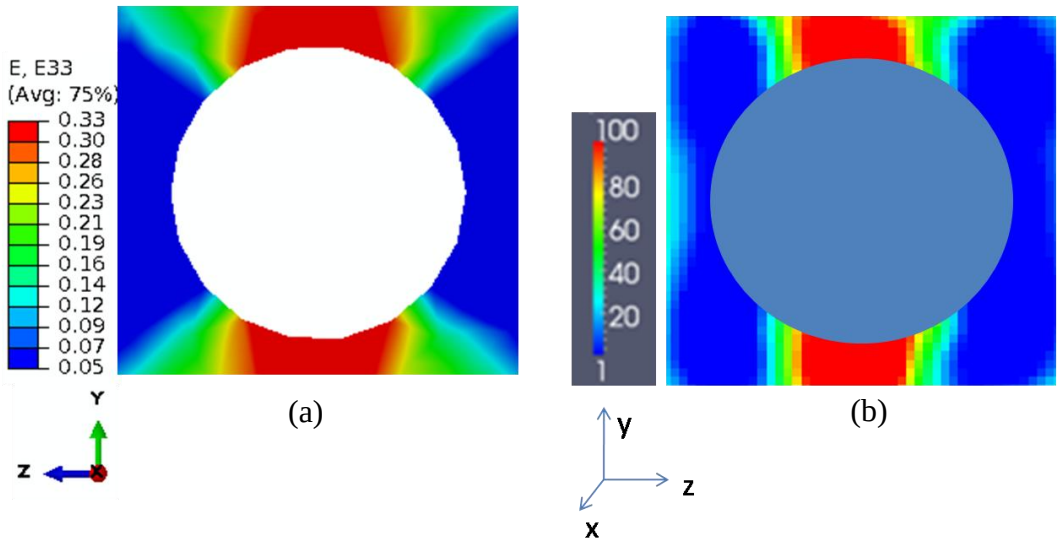

Figure 31 Strain E33 as predicted by (a) FE Model (b) DIC code

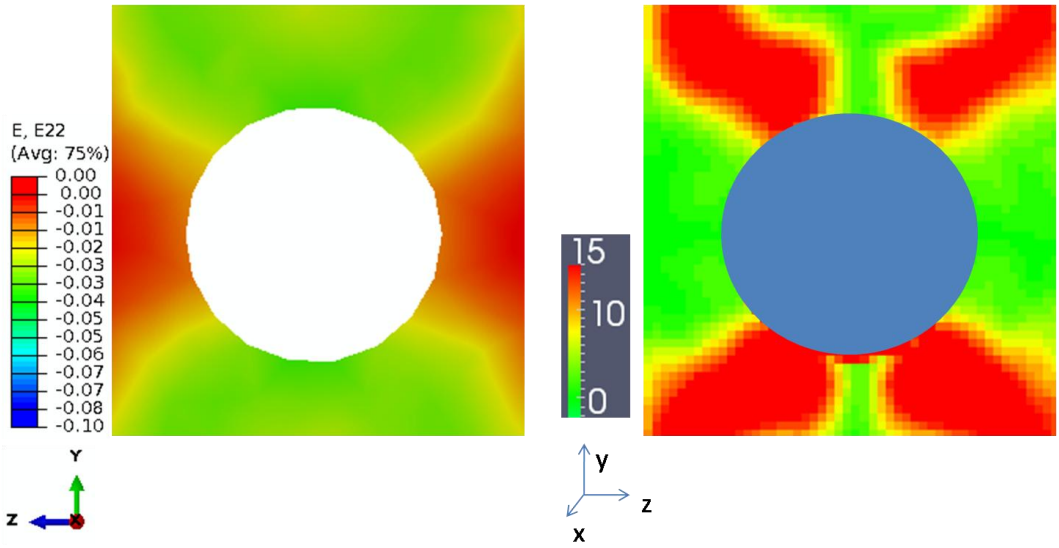

Figure 32 Strain E22 as predicted by (a) FE Model (b) DIC code (The difference in color contours is due to the difference in the scale bars)

Chapter 6

SUMMARY

In this research, three dimensional finite element analysis of Pb-free solder joints incorporating the exact geometry of the pores was carried out to understand the influence of porosity on the deformation behavior as well as overall failure of the joint. A damage model was incorporated in the analysis to predict crack nucleation and propagation path in the joint. The analysis results were validated by comparing the model predictions with the actual results obtained by the interrupted experiment. The simulation results showed a very good correlation with the experimental results. The deformation of the pores predicted the numerical model was in very close agreement with the tomographic observations. The simulated crack nucleation site as well as the propagation path compared very well with the actual crack path. The validated FE model was then used to simulate the failure of different solder joints with varying degrees of porosity to understand the influence of different void characteristics on the failure of the joints. It was observed that for joints with more than 1% void volume fraction, the strength was reduced considerably. Another factor that affected the failure pattern was the geometry of the joint. For one of the samples, it was observed that the highly necked central region of the joint had more influence on the eventual failure path than the pores in the joint. Thus, this study enabled visualization of failure of solder joints under the influence of varying degree of porosity.

In this research, a three dimensional digital image correlation technique was implemented in MATLAB which can be used as an efficient tool to measure

the experimental displacement and strain. The accuracy of the tool was demonstrated by considering a model test case. The 3D DIC code predicted the deformation of the model quite accurately.

Future work for this research would include modeling of the entire electronic package to determine the most critical solder balls in the package. Also, to test the 3D DIC code for more complex cases.

REFERENCES

Aspandiar, R. *Voids in Solder Joints.* Northwest Chapter Meeting, Septemeber: Technical Report,Intel Corporation, 2005.

Baruchel, J., et al. "Advances in synchrotron hard X-ray based imaging." *Comptes Rendus Physique* 9, no. 5-6 (2008): 624-641.

Bath, J. "A Manufacutrable Lead Free Surface Mount Process?" *Circuit Assembly*, 2003: 26-30.

Bay, B K, T S Smith, D P Fyrhie, and M Saad. "Digital Volume Correlation: Three-dimensional Strain Mapping using X-Ray Tomography." *Experimental Mechanics* 39, no. 3 (1998): 219-226.

Benouali, A, Y Froyen, J F Delerue, and M Wevers. "Mechanical and microstructural characterization of metal foams." *Material Science and Technology* 18, no. 5 (2002): 489-494.

Chan, Y C, D J Xie, and J Lai. *Material Science Engineering B* 38 (1996): 53-62.

Chawla, N., R. Sidhu, and V. Ganesh. *Acta Materialia* 54 (2006): 1541-1548.

Chu, T C, W F Ranson, and M A Sutton. "Applications of digital image correlation techniques to experimental mechanics." *Experimental Mechanics* 25 (1985): 232-244.

Dassault Systems Simulia. "Abaqus 6.9 User's Manual." 2010.

Doroszuk, A, et al. "BGA Solder Joint Void and Its Effect on Thermal Fatigue." Chicago, 2000.

Dudek, M, Luke Hunter, J J Williams, S H Lau, S Kranz, and N Chawla. "Three dimensional visualization of reflow porosity and modeling of deformation in Pb-free solder joints." *Materials Characterization* 61 (2010): 433-439.

Dudek, M., and N. Chawla. "Three-dimensional (3D) microstructure visualization of LaSn3 intermetallics in a novel Sn-rich rare-earth-containing solder." (Materials Characterization) 59, no. 9 (2008): 1364-1368.

Germaneau, A, P Doumalin, and J C Dupre. "Full 3D Measurement of Strain Field by Scattered Light for Analysis of Structures." *Experimental Mechanics* 47 (2007): 523-532.

Gonzalez, M, B Vandevelde, J Vanfleteren, and D Manessis. "Thermo-Mechanical FEM Analysis of Lead Free and Lead Containing Solder for Flip Chip Applications." Brugge,Belgium: EMPC, 2005.

Herzog, T, K J Wolter, and F Poetsch. "Investigation of Void Formation and Shear Strength of Sn42Bi58 Solder Joints for Low Cost Applications." New Orleans, 2003. 1738-1745.

Huang, B, A Dasgupta, and N C Lee. "Effect of SAC Composition on Soldering Performance." NJ: IEEE, SEMI International Electronic Manufacturing Symposium, 2004. 45-55.

Jandejsk, I, O Jirousek, and D Vavrik. "Precise strain measurement in complex materials using Digital Volumetric Correlation and time lapse micro-CT data." *Procedia Engineering* 10 (2011).

Kim, D, T Shibutani, and Q Yu. "Effect of Void Formation on Thermal Fatigue Reliability of Lead-Free Solder Joints." Las Vegas: Inter Society Conference on Thermal Phenomena, 2004. 325-330.

Kinney, H., and C. Nichols. "X-ray tomographic microscopy (XTM) using synchrotron radiation." *Annual Review of Materials Science* 22, no. 1 (1992): 121-152.

Kubis, J., J. Shiflet, and R. Hull. "Focused Ion Beam Tomography." *Metallurgical and Materials Transaction A* 35, no. 7 (2004): 1935-1943.

Ladani, L, and A Dasgupta. "Effect of Voids on Thermo-Mechanical Durability of Pb-free BGA solder Joints: Modeling and Experiment." (Journal of Electronic Packaging) 129 (2007): 273-278.

Lau, J H, and C G Harkins. "Thermal Stress Analysis of SOIC Packages and Interconnections." (IEEE Transactions Components, Hybrids Manufacturing Technology) 11, no. 4 (1998): 380-389.

Lau, J, and S Eramus. "Effects of Voids on Bump Chip Carrier (BCC++) Solder Joint Reliability." San Diego: IEEE Electronic Components and Technology Conference, 2002. 992-998.

Lee, N C. "Reflow processing and Troubleshooting SMT,BGA,CSP and Flip Chip Technologies." Newnes,Boston, 2002.

Lee, S, G Kim, B Han, and M Cho. "Strain measurement from 3D micro-CT images of a breast-mimicking phantom." *Computers in Biology and Medicine*, 2011.

Lee, T, J Lee, and I Jung. "Finite element analysis for solder ball failures in chip scale package." *Microelectronics and Reliability* 38, no. 12 (1998): 1941-1947.

Liu, S, and Y H Mei. "Effect of Voids and their Interactions on SMT Solder Joint Reliability." (Soldering Surface Mount Technology) 6, no. 18 (1994): 21-28.

Maire, E, Y Buffiere, L Salvo, J Blandin, W Ludwig, and J Letang. "On the application of X-Ray Micro-Tomography in the field of materials science." *Advanced Engineering Material* 3, no. 8 (2001): 539-546.

Pan, B, A Asundi, H Xie, and J Gao. "Digital image correlation using iterative least squares and point wise least squares for displacement field and strain field measurements." *Optics and Lasers in Engineering* 47 (2009): 865-874.

Pan, B, K Qian, H Xie, and A Asundi. "Two dimensional digital image correlation for in-plane displacement and strain measurement." *Measurement Science and Technology* 20 (2009).

Peter, W H, and W F Ranson. "Digital Imaging Techniques using Experimental Stress Analysis." *Opt Eng* 21 (1982): 427-431.

Phillips, D H, and J J Lanutti. "Measuring physical density with X-Ray computed tomography." *Non-Destructive Testing and Evaluation Int* 30 (1998): 339-350.

Shen, Y L. "Inelastic Deformation,Course Pack: MSE 561 Speacial Topics." 2008.

Shen, Y, and K Aluru. "Numerical study of ductile failure morphology in solder joints under fast loading condition." *Microelectronics Reliability* 50 (2010): 2059-2070.

Shen, Y, N Chawla, E Ege, and X Deng. "Deformation analysis of lap-shear testing of solder joints." *Acta Materialia* 53 (2005): 2633-2642.

Sidhu, R., and N. Chawla. "Three Dimensional Microstructure Characterization of Ag3Sn Intermetallics in Sn-rich solder by serial sectioning." *Materials Characterization* 52, no. 3 (2004).

Silva, F, J Williams, M Muller, M Hentschel, P Portella, and N Chawla. *METALLURGICAL AND MATERIALS TRANSACTIONS A* 41A (2010).

Singh, DRP, and N. Chawla. "Focused Ion Beam (FIB) tomography of nanoindentation damage in nanoscale metal/ceramic multilayers." *Materials Characterization* 61, no. 4 (2010): 481-488.

Smetana, J, et al. "Desgin, Materials and Process for Lead Free Assembly of High Density Packages." (Sodering and Surface Mount Technology) 16, no. 1 (2004): 53-62.

Smith, T, B Bay, and M Rashid. "Digital Volume Correlation Including Rotational Degrees of Freedom during Minimization." *Experimental Mechanics* 42 (2002).

Stafstrom, E, A Singer, A McLenaghan, and K Nishu. "Reducing Solder Voids with Copper Filled MicorVias." *Cicuits Assembly* 14, no. 4 (2003): 22-24.

Sutton, M, W Wolters, W Peter, W Ranson, and S McNeill. "Determination of displacements using an improved digital correlation method." *Image Vision Computing* 1 (1983): 133-139.

Tang, Z, and F Shi. (Microelectronic Journal) 32, no. 7 (2001).

Tanie, T, and H Terasaki. "Fatigue Crack Propagation Analysis for Micro Solder Joints with Void." International Symposium on Electronics Materials and Packaging, 2005.

Verhulp, E, B Rietebergen, and R Huiskes. "A three dimensional Image Correlation Technique for strain measurement in microstructures." *Journal of BioMechanics* 34 (2004).

Williams, J., Z Floma, A Amella, and X Xiao and F De Carlo N Chawla. *Acta Materialia* 58, no. 18 (2010): 6194-6205.

Yu, Q, T Shibutani, D Kim, Y Kobayashi, and J Yang. "Effect of process-induced voids on isothermal fatigue resistance of CSP Lead Free Solder Joints." *Microelectronics Reliability* 48 (2008): 431-437.

Yunus, M, K Srihari, J Pitaressi, and A Primavera. (Microelectronic Reliability) 43, no. 12 (2007): 2077-2086.

Yunus, M, K Srihari, J Pitaressi, and A Primavera. "Effect of voids on the reliability of BGA/CSP solder joints." *Microelectronics Reliability* 43 (2003): 2077-2086.

Zhu, N. Annual IEEE Semiconductor Thermal Measurement Management Symposium, 1999. 22-29.

Zhu, W, S Stoeck, H Pape, and S Gan. "Comparative Study On Solder Joint Reliability Using Different FE-Models." (IEEE ElectronicPackaging Technology Conference) 2003: 687-694.